Notch2 signaling guides B cells away from germinal centers towards marginal zone B cell and plasma cell differentiation

T. Babushku[1,2], S. Rane[3], M. Lechner[1], A. J. Yates[4], U. Zimber-Strobl[1,2*#], L. J. Strobl[1#]

[1]Research Unit of Gene Vectors, Research Group B Cell Development and Activation, Helmholtz Center Munich, German Research Center for Environmental Health GmbH, Feodor-Lynen-Str. 21, D-81377 Munich, Germany.

[2]TranslaTUM, Center for Translational Cancer Research, Technical University of Munich, Einsteinstraße 25, D-81675 Munich, Germany.

[3] Irving Institute for Cancer Dynamics, Columbia University, 1190 Amsterdam Ave, New York 10027, USA

[4]Department of Pathology and Cell Biology, Columbia University Irving Medical Center, 630 West 168th Street, New York, NY 10032, USA

* Corresponding author: Ursula Zimber-Strobl, e-mail: strobl@helmholtz-muenchen.de

[#] these authors contributed equally

Abstract

Notch2 signaling has a profound role in driving the development of marginal zone B (MZB) cells. We recently demonstrated that follicular B (FoB) cells act as precursors for MZB cells in mice, but the mechanistic aspects of this differentiation pathway are still elusive. Our current study revealed that Venus expression in CBF:H2B-Venus reporter mice, which is a proxy for Notch signaling, increases progressively with B cell maturation and is highest in MZB cells, suggesting that most peripheral B cells receive a Notch signal and cells with the highest signal preferably develop into MZB cells. Strikingly, Venus expression was heterogeneous in the MZB pool, indicating a loss of Notch signaling over time. In addition, our data revealed an interplay between antigen induced activation and Notch2 signals, in which FoB cells that turn off the Notch pathway enter GC reactions, whereas B cells with high Notch signals undergo MZB and plasmablast differentiation. Integration of our experimental data into a mathematical modeling framework revealed that antigen activation induces a binary cell-fate decision in FoB cells, to differentiate into either GC or MZB cells. The newly generated MZB cells have a short life span and are sustained by the influx of antigen activated B cells. Our analyses demonstrate that MZB cell generation is a systematic response to TD immunization and provide for the first time a detailed quantitative map of their dynamics during an ongoing TD immune response.

One-sentence summary: Notch2 signaling acts as binary switch in antigen-activated FoB cells, preventing entry into GCs and instead inducing development into plasmablasts and MZB cells.

Introduction

Mature splenic B2 lymphocytes are comprised of two distinct cell populations: Follicular B (FoB) and Marginal Zone B (MZB) cells. FoB cells recirculate between lymphoid organs, whereas MZB cells are mostly sessile in the marginal zone (MZ) and can occasionally migrate between the B cell follicle and the MZ (1). MZB cells respond to T-cell-independent (TI) antigens by differentiation into low affinity IgM-producing plasma cells (PCs) (2, 3). In contrast, FoB cells respond to T-cell-dependent (TD) antigens, giving rise to germinal centers (GC), where they undergo class switching and somatic hypermutation, resulting in the generation of high-affinity Ig-switched PCs and memory B cells (4).

B cell development begins in the bone marrow (BM) and is completed in the spleen. Immature B cells leave the BM upon successful rearrangement of the B-cell-receptors (BCR), and transition through short-lived developmental stages (T1-T3) before undergoing a binary fate decision to differentiate into either FoB or MZB cells in the spleen (5-7). MZB cells may also develop from FoB cells, in particular FoB-II cells, a recirculating long-lived population with an $IgM^{high}IgD^{high}CD21^{int}CD23^{+}$ phenotype (8-12). We recently strengthened this hypothesis by showing that the adoptive transfer of highly purified FoB cells into immunocompetent recipients led to the generation of donor-derived MZB cells via an intermediate MZ precursor stage (13). Our data provided strong evidence that FoB cells can act as precursors for MZB cells and we postulated that this could be physiologically mediated via activation of Notch2.

Notch2 signaling has been long known to be a crucial player in MZB cell development. Constitutively active Notch2 signaling in T1 or FoB cells strongly induces MZB cell differentiation (13, 14). In contrast, homozygous or heterozygous inactivation of Notch2 in B lymphocytes or of its ligand Dll-1 in non-hematopoietic cells leads to the total loss or reduction of MZB cells, respectively (15, 16), suggesting a dependence of MZB cell development on

ligand/receptor dosage. This phenomenon may imply that the bottleneck in MZB cell development is the extent of Notch2 signaling, which is modulated by Notch2 surface expression and its modification (15, 17, 18) as well as the availability of Dll-1-expressing fibroblasts (19). Additionally, BCR-signaling strength has been assumed to influence MZB cell fate decisions (5, 20). We have shown that Notch2 surface expression is strongly upregulated by BCR-stimulation *in vitro* (13) and others found that BCR-signaling induces recruitment of Adam10 to the plasma membrane, enhancing the cleavage and subsequent activation of Notch2 (21). These findings suggest that BCR signals act upstream of Notch2 signaling and in combination with CD40 signals, increase the likelihood of B cells to acquire a strong Notch2 signal that drives their differentiation to MZB fate.

By studying Venus expression in different B cell populations of Notch-reporter mice, we now demonstrate that almost all B cells receive a Notch signal under steady-state conditions, and this signal is strongest in MZB cells. Moreover, we provide evidence that induction of Notch2 signaling upon TD immunization navigates cells away from the GC reaction and induces PC and MZB cell differentiation instead, thus making the Notch2 signaling pathway an important binary switch between opposed B cell fates.

Results

All B2 lymphocytes receive a Notch signal under steady-state conditions

To identify the B cell populations that receive a Notch signal, we analyzed B lymphocytes in the BM and spleen of CBF:H2B-Venus mice (22), which express Venus in all cells that receive a Notch signal. We found that almost all developing B c

ell populations in the BM were Venus^{+}, with recirculating B cells (CD43^{-}B220^{high}) having the highest Venus expression (Fig. 1A).

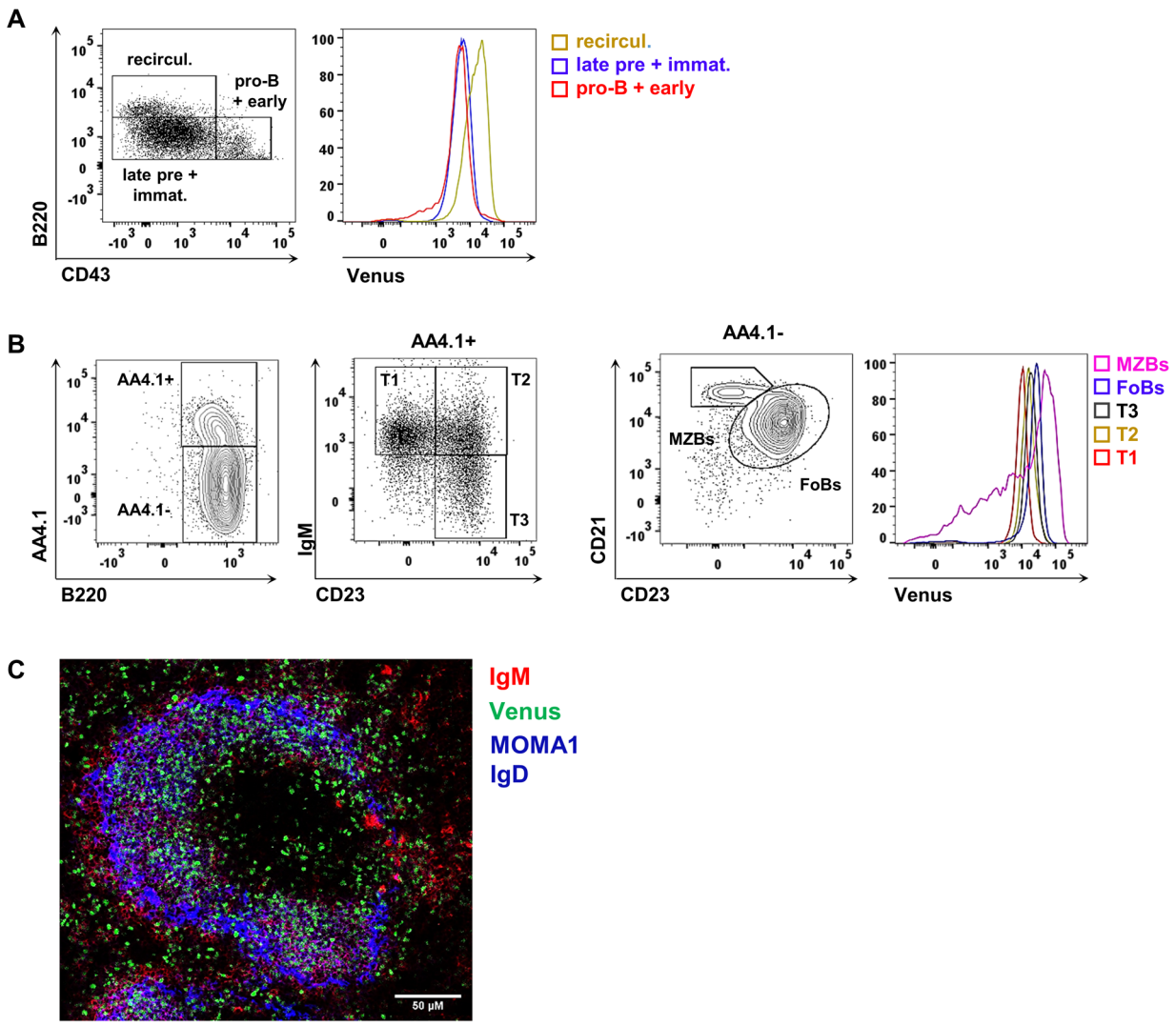

Fig. 1. All B2 lymphocytes receive a Notch signal. (A) Live B220^{+} lymphocytes in the BM of CBF:H2B-Venus mice were subdivided in pro- and early pre- (CD43^{+}B220^{low}), late pre- and immature (CD43^{low}B220^{low}) and recirculating (CD43^{-}B220^{high}) B cells. **(A-B)** The histogram overlays show Venus expression in the gated cell populations. n=5. **(B)** Splenic transitional B cells were gated as AA4.1^{+}B220^{+} and subdivided into T1-T3 cells according to their CD23/IgM expression. Mature B cells were gated as AA4.1^{-}B220^{+} and further separated into FoB (CD23^{+}CD21^{low}) and MZB cells (CD23^{low}CD21^{high}). **(C)** Immunofluorescence analysis of splenic sections, stained for MZB cells (IgM^{+}, red), FoB cells (IgD^{+}; blue) and metallophilic macrophages (MOMA1^{+}; blue). Green dots represent Venus-expressing cells. n=3.

In the spleen, Venus expression gradually increased from T1 over T2 to T3 cells, and continued to increase in FoB and MZB cells. Although Venus expression was the highest in MZB cells, a subset of them expressed less Venus than the majority of B cells in the spleen, suggesting

that some MZB cells downregulate or turn off Notch signaling over time (Fig. 1B). This observation was recapitulated by our immunohistochemical staining, which showed that some MZB cells are indeed Venus^{-} (Fig. 1C).

Notch2 signaling is downregulated in most GCB cells and PCs

To analyze activity of Notch2 signaling in B cell populations that specifically arise during the primary immune response to a TD antigen, we injected CBF:H2B-Venus mice with 4-Hydroxy-3-nitrophenylacetyl-Chicken Gamma Globulin (NP-CGG) and subsequently analyzed them 7- and 14-days post immunization (p.i.). The Venus signal was progressively downregulated in most GC B cells, compared to non-GCB cells (Fig. 2A). Furthermore, we found that only a small number of GCB cells were still Venus^{high}, with a higher percentage of Venus^{high} cells at day 7 than at day 14 p.i. (Fig. S1A). Also, in immunohistochemistry, the GC structures were mostly Venus^{-}, with only a few Venus^{bright} GL7^{+} cells detected. (Fig. 2B). By day 14, the Venus^{high} GCB cells were substantially enriched in the light zone (LZ), whereas Venus^{mid} and Venus^{neg} cells were preferentially found in the dark zone (DZ) (Fig. S1B). Venus expression was strongly reduced in most TACI^{+}CD138^{+} PCs (Fig. 2C) and histology for Irf4-expressing cells confirmed this finding (Fig. 2D). Although most PCs had completely shut off the Venus signal, a small portion of TACI^{+}CD138^{+} cells remained Venus^{high}. Most of these cells also expressed CD19 and B220, suggesting they were (pre-) plasmablasts rather than mature PCs (Fig. 2C).

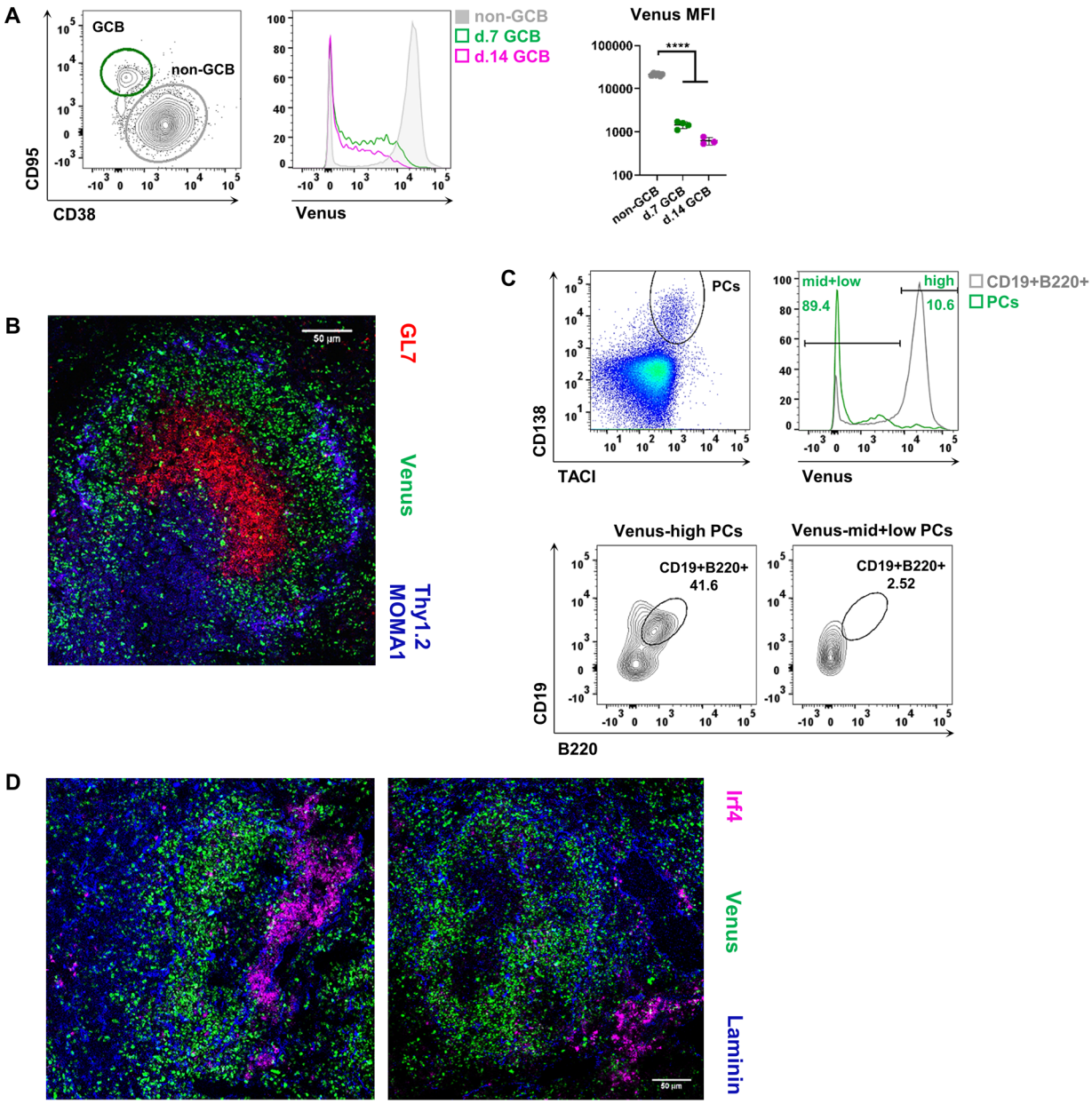

Fig. 2. Notch signaling is downregulated in most GCB cells, and mature PCs. (A) FACS plots are pre-gated on live B lymphocytes and show the gating of GC ($CD95^{high}CD38^{low}$) and non-GCB ($CD95^{low}CD38^{+}$) cells (day 7 p.i.) n≥3. The histogram shows an overlay of the Venus expression in GCB and non-GCB cells. The graph summarizes median fluorescent intensities (MFI) of Venus in the analyzed populations. ****p<0.0001, Tukey's one-way ANOVA of logarithmized MFI values. **(B)** Sections were stained for GCs ($GL7^{+}$; red), T cells ($Thy1.2^{+}$; blue) and metallophilic macrophages ($MOMA1^{+}$; blue) 7 days p.i. Scale bar represents 50 µm. n=2. **(C)** Splenocytes were pre-gated using a large lymphocyte gate and analyzed for PCs ($TACI^{+}CD138^{+}$). The histogram shows an overlay of Venus expression in PCs and $B220^{+}CD19^{+}$ B cells, gates and percentages refer to the green histogram of the

PCs, gated as in the plot. Contour plots depict the CD19/B220 expression in Venus^{high} and Venus$^{mid+low}$ PCs (TACI^{+}CD138^{+}). **(D)** Staining of splenic sections to detect plasmablasts and PCs (Irf4^{+}; pink) and basement membranes of endothelial cells (Laminin; blue) at 7 days p.i. Scale bar represents 50 µm. n=2.

Generation of GCB cells is impaired by Notch2IC induction

Our data revealed that most B cells receive a Notch signal, but Notch signaling is downregulated in the GC. To further study the influence of Notch signaling on the GC reaction, we immunized conditional transgenic mice in combination with the Cγ1-Cre strain (23), in which the Notch2-receptor is deleted (N2KO//CAR) or constitutively activated by expression of the intracellular part of Notch2 (N2IC/hCD2) upon TD immunization with NP-CGG. As controls, we used control/CAR mice, in which the reporter human coxsackie/adenovirus receptor (CAR) is expressed upon Cre-mediated recombination (24). To trace the B cells that successfully underwent Cre-mediated recombination, we used the reporter gene CAR in the N2KO//CAR and control/CAR mice, and hCD2 in N2IC/hCD2 mice. The mouse strains are described in Materials and Methods and in Fig. S2A in more detail.

Following intraperitoneal NP-CGG injection, reporter^{+} B cells were detected in the spleen at day 7 p.i. with NP-CGG. The deletion efficiency of the targeted regions was comparable in all three mouse strains. The amounts of reporter^{+} cells peaked at day 14 with around 5-6%, followed by a decline to 2% at day 30 (Fig. S2B). Although all mice had similar percentages of reporter^{+} B cells, mice with induced Notch2IC-expression were unable to generate GCB cells (Fig. 3A). Thus, only a few GCB cells could be detected in these animals, most of which were reporter^{-} (Fig. 3B). In addition, immunohistochemistry revealed only small GC structures, which were not localized at the T-/B-cell border in N2IC/hCD2 mice (Fig. 3C). In contrast, N2KO//CAR and control/CAR mice generated similar percentages of GCB cells, which

clustered into structures with correct localization inside the splenic follicle at the B/T cell border (Fig. 3A-C). These data suggest that functional Notch2 signaling is not necessary for GCB cell differentiation, and even interferes with proper GC formation.

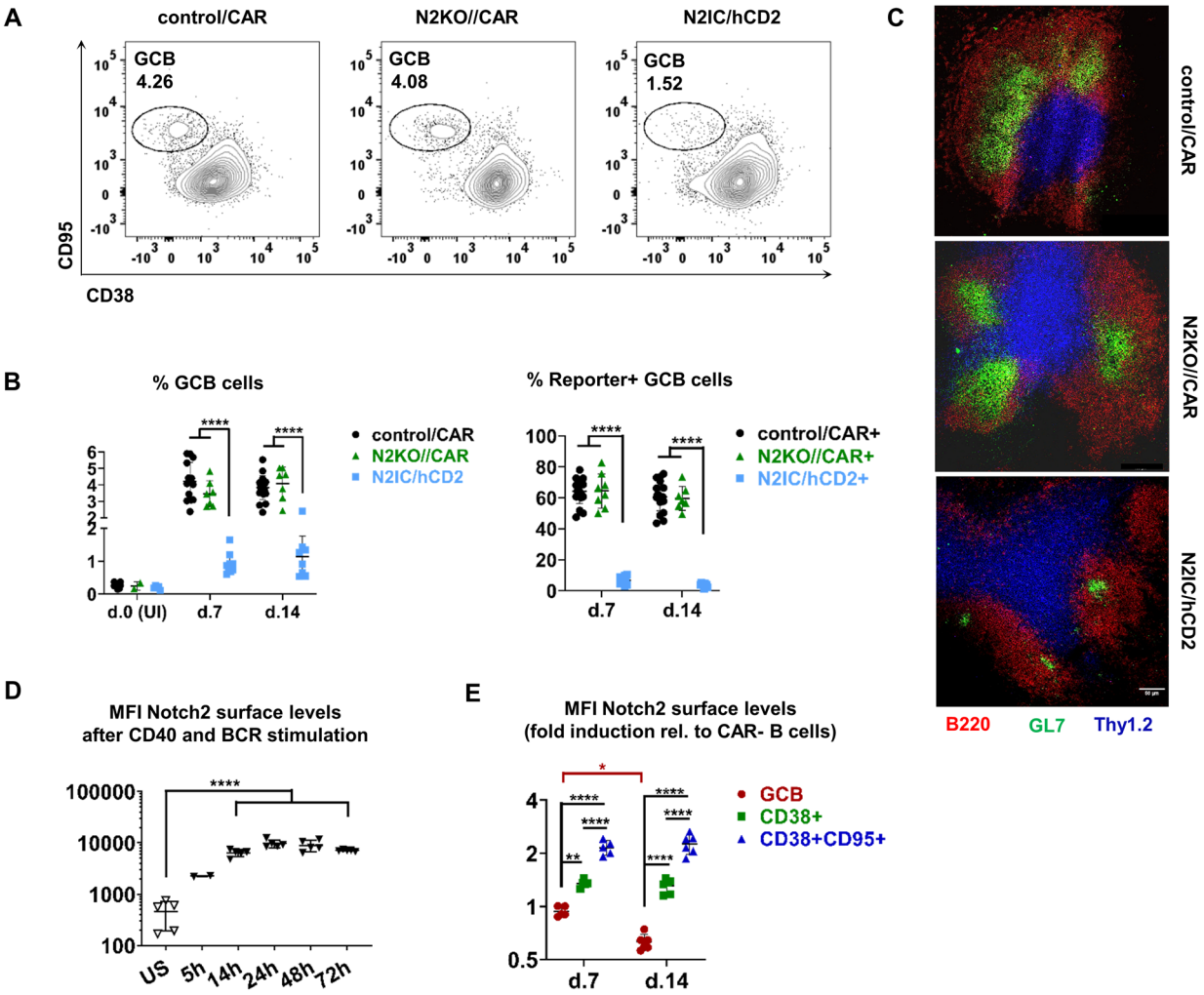

Fig. 3. Antigen-induced Notch2IC-expression inhibits GC formation (A) Splenic B220^{+} B cells were analyzed for GCB cells (CD95^{+}CD38^{low}). FACS plots are pre-gated on live B lymphocytes and are representative for day 7 p.i.. **(B)** The graph on the left compiles the percentages of total GCB cells in the spleen of mice from the indicated genotypes at the indicated time points p.i.. The graph on the right shows a summary of the percentages of reporter^{+} GCB cells. d0 n=10/2/5, d7 n=14/7/9, d14 n=20/7/8 for control/CAR+/N2KO//CAR+/N2IC/hCD2+, respectively, ****p≤0.0001, ordinary 2-way-ANOVA, Tukey´s multiple comparison test. **(C)** Splenic sections from mice of the indicated genotypes 7 days p.i.. Sections were stained for GCB cells (GL7^{+}; green), B cells (B220^{+}; red) and T cells (Thy1.2^{+}; blue). Scale bar represents 50 µm. n=4. **(D)** Graphical summary of median fluorescent intensities (MFI) of Notch2 cell surface expression on purified FoB cells at indicated time points after α-IgM and α-CD40 stimulation. n=5, except for 5h where n=2. ****p ≤ 0.0001, Tukey's 1-way-

ANOVA. **(E)** Fold induction of Notch2 (MFI) in the control/CAR$^+$ CD38/CD95 subpopulations relative to its expression (MFI) in CAR$^-$ B cells. d7 n=5, d14 n=6. *p=0.011, **p=0.001 and ****p≤0.0001, Sidak's 2-way-ANOVA.

Notch2 surface expression is upregulated on activated FoB cells of control/CAR animals

Next, we analyzed whether cell surface expression of Notch2 varies across B cell subsets derived from control/CAR animals. We found an around 20-fold upregulation of Notch2 on the cell surface of FoB cells upon combined CD40- and BCR-stimulation *in vitro*. This upregulation started early and peaked between 24h and 48h of stimulation (Fig. 3D, S3A). Notch2 surface expression was also upregulated upon TD immunization *in vivo*. Thus, Notch2-receptor-expression was approximately 2-fold upregulated in reporter$^+$CD38$^+$CD95$^+$ non-GCB cells in comparison to reporter$^-$ B cells, while CD38$^-$CD95$^+$ GCB cells progressively downregulated Notch2-surface expression over time post immunization (Fig. 3E, S3B). Thus, our *in vitro* and *in vivo* data suggested that Notch2 surface expression is induced on activated non-GCB cells, whereas it is downregulated in fully differentiated GCB cells, consistent with the low levels of Venus expression in GCB cells from immunized CBF:H2B-Venus mice.

N2IC-expressing cells upregulate Irf4, but fail to induce Bcl6

Although N2IC/hCD2 mice did not form GCs, they had similar frequencies of reporter$^+$ B cells as control/CAR animals. Most of them expressed high CD38 levels, but varied in their expression of CD95 (Fig. 4A-B). Intracellular staining for the transcription factors Irf4 and Bcl6, which are key regulators of PC- and GC-differentiation respectively, revealed an inverse regulation in N2IC/hCD2 and control/CAR mice. Most control/CAR$^+$ B cells strongly induced Bcl6 expression, but kept Irf4 levels very low, consistent with their GCB cell phenotype. In contrast, N2IC/hCD2$^+$ B cells did not upregulate Bcl6, but showed a strong induction of Irf4 (Fig. 4C).

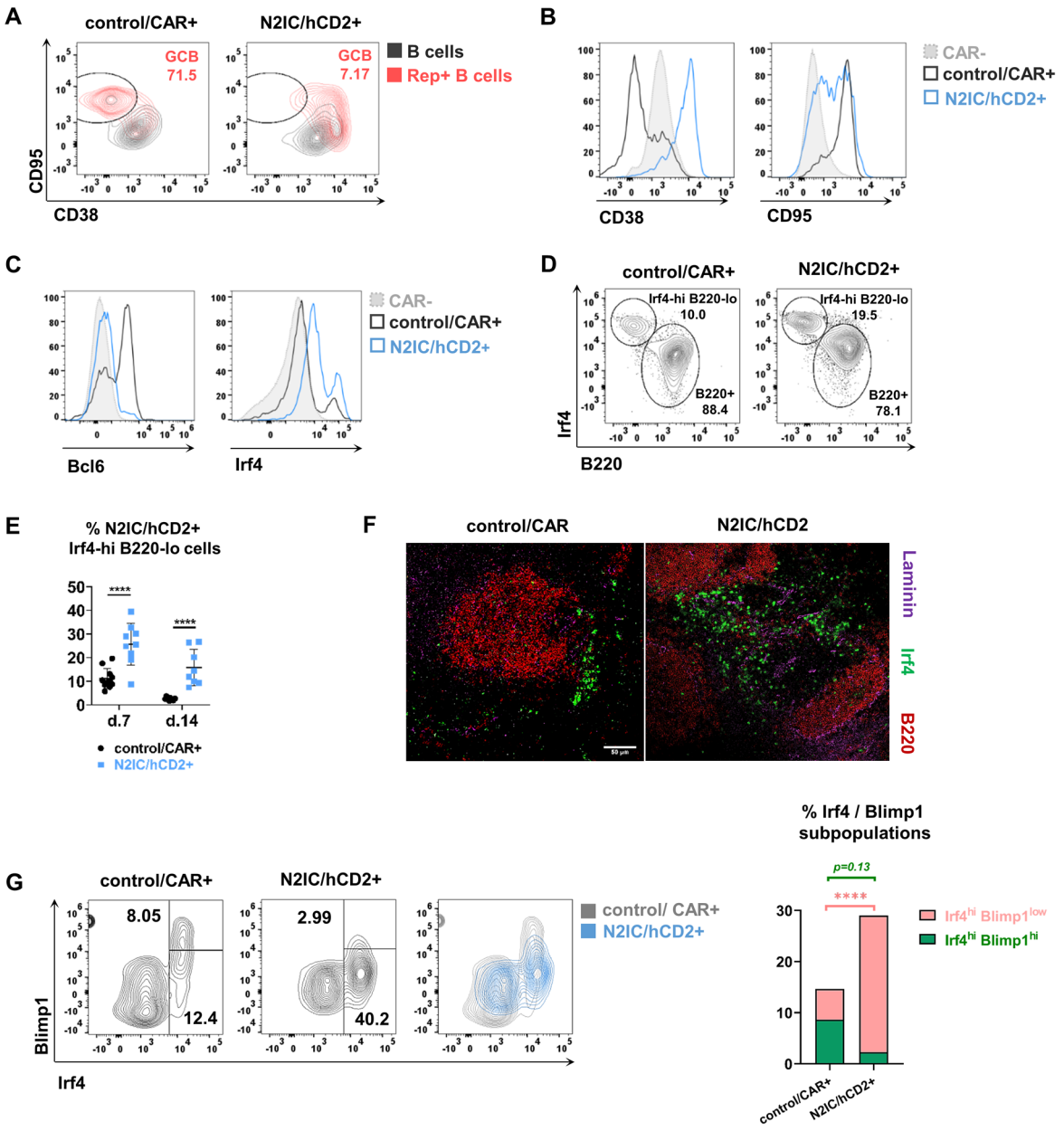

Fig. 4. N2IC/hCD2$^+$ cells upregulate Irf4, but fail to induce Bcl6. FACS plots are pre-gated on live lymphocytes (day 7 p.i.). n≥6. **(A)** Splenic reporter$^+$B220$^+$ B cells were analyzed for their GCB cell phenotype (CD95$^+$CD38^{low}). Overlays between reporter$^+$ B cells and total B220$^+$ cells are shown. Gates and percentages refer to the reporter$^+$ population. **(B)** Histograms depict the overlays of CD38 and CD95 expression in reporter$^+$ B cells from N2IC/hCD2 and control/CAR mice, compared to reporter$^-$ B cells. **(C)** Histograms show the overlay of Bcl6 and Irf4 expression in reporter$^+$ lymphocytes and reporter$^-$ lymphocytes. **(D)** Irf4/B220 expression in reporter$^+$ lymphocytes. Two subpopulations were identified: Irf4^{high}B220^{low} and Irf4^{mid}B220$^+$. **(E)** Summary graph depicting the percentages of reporter$^+$Irf4^{high}B220^{low} cells at indicated time points. ****p<0.0001, Sidak's 2-way-ANOVA. **(F)** Immunofluorescence analysis of splenic sections, stained for (pre-) plasmablasts and plasma cells

(Irf4^{high}; green) and B cells (B220^{+}; red). Scale bar represents 50 µm. n=3. **(G)** The staining was performed after fixation and permeabilization of cells. Reporter^{+} cells were separated into Blimp1^{high}Irf4^{high} mature PCs and Blimp1^{low}Irf4^{high} plasmablasts. The overlay shows the Irf4/Blimp1 expression of control/CAR^{+} and N2IC/hCD2^{+} cells. The stacked bar chart compiles the percentages of Blimp1^{high}Irf4^{high} and Blimp1^{low}Irf4^{high} cells at day 7 p.i. n=5. ****p<0.0001, Sidak's 2-way-ANOVA.

Even though most N2IC/hCD2^{+} cells were Irf4^{+}, there was a second fraction, which was Irf4^{high}. This fraction was also detected in reporter^{+} cells from control/CAR mice but at a lower frequency. The Irf4^{high} cells were uniformly B220^{-} in both genotypes (Fig. 4D and E), pointing to a plasmablast/PC phenotype. Immunohistochemistry revealed that the enriched Irf4^{high} cells were predominantly located in the extrafollicular regions between neighboring B cell follicles, where plasmablasts and short-lived PCs are usually located (Fig. 4F).

Notch2IC-expression enhances plasmablast differentiation

Further characterization of the Irf4^{high}B220^{-} cells revealed that, in comparison to controls, the Notch2IC-expressing Irf4^{high}B220^{-} cells had lower Blimp1 levels, indicating that they were arrested at the plasmablast stage and did not develop into mature PCs (Fig. 4G). This observation is consistent with the data from Notch-reporter mice, which displayed high levels of Venus in pre-plasmablast and plasmablasts, but low levels in terminally differentiated PCs. ELISpot analyses with splenic B cells revealed increased abundance of NP-specific IgM cells, but severely reduced NP-specific IgG1 and IgG3 cells in N2IC/hCD2 mice related to controls at day 7 p.i. (Fig. S4A). A similar trend was visible in the BM, where frequencies of NP-specific IgM^{+} cells were increased and the frequencies of IgG1^{+} cells were decreased (Fig. S4B). In the sera, NP-specific IgM titers were comparable whereas IgG1 titers were decreased in N2IC/hCD2 mice related to control/CAR mice (Fig. S4C). In summary, these data suggest that a strong Notch signal drives cells towards extrafollicular plasmablast differentiation, most of which are short-lived (Blimp1^{low}), unswitched, IgM-producing cells.

Some antigen-activated N2IC-expressing B cells differentiate into MZB cells

In contrast to control animals, Irf4^{mid}B220^{+} cells in N2IC/hCD2 mice were clearly Bcl6^{-} and expressed higher levels of Irf4 (Irf4^{mid}) (Fig. 5A-B). Considering the role of induced constitutively active Notch2 signaling in the differentiation of FoB into MZB cells under steady-state conditions (13), we analyzed whether these cells adopt a MZB cell phenotype over time. Indeed, at day 7 post-immunization, around one-fourth of N2IC/hCD2^{+}Irf4^{+}B220^{+} cells had a MZB cell phenotype according to their CD21/CD23 surface expression (Fig. 5C). Frequencies of N2IC/hCD2^{+}CD21^{high}CD23^{low} cells increased with time after immunization (Fig. 5D, S5). In parallel, these cells also increased their size (FSC) and upregulated IgM, CD1d and CD38 (Fig. 5E), which is fully in accord with the published MZB cell surface phenotype (CD23^{low}CD21^{high}IgM^{high}CD1d^{high}CD38^{high}). Moreover, the N2IC-expressing cells migrated towards the marginal zone. Some N2IC/hCD2^{+} cells were still located within the follicle at day 7. However, with ongoing time post immunization, progressively more of these cells were localizing in the MZ (Fig. 5F). By day 30, most of the N2IC/hCD2-expressing cells were at their defined splenic location, forming a MZ ring around the follicle. Together, our data imply that Notch2IC induction in FoB cells upon TD antigen activation not only caused a shift towards the MZB cell surface phenotype, but also guided the newly generated MZB cells to their correct splenic localization.

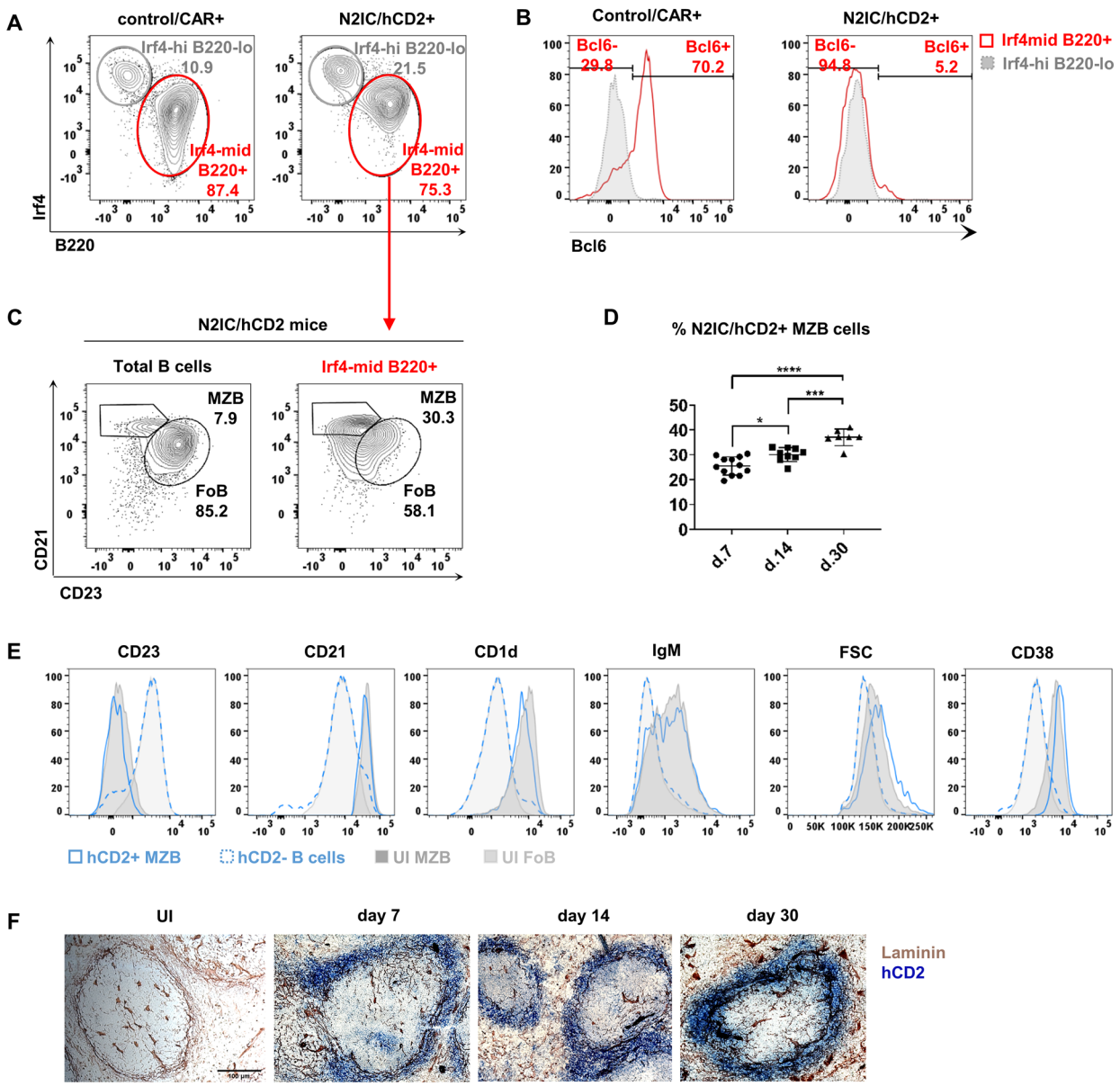

Fig. 5. N2IC/hCD2^{+} B cells differentiate into MZB cells with the correct surface phenotype and splenic localization. (A) Reporter^{+} lymphocytes were separated into B220^{low}Irf4^{high} and B220^{+}Irf4$^{mid/low}$ cells. FACS plots are pre-gated on reporter^{+} live lymphocytes. **(B)** Histograms show overlays of Bcl6 expression in reporter^{+}B220^{+}Irf4^{mid} and B220^{low}Irf4^{high} cells. **(C)** Gating of MZB (CD21^{high}CD23^{low}) and FoB (CD23^{high}CD21^{low}) cells in N2IC/hCD2 mice. The left plot is gated on B220^{+} cells, and the right plot on N2IC/hCD2^{+}B220^{+}Irf4^{mid} cells. **(A-C)** FACS plots are representative for day 7 p.i. n≥4. **(D)** Graphical summary of the percentages of N2IC/hCD2^{+}CD21^{high}CD23^{low} MZB cells at indicated time points. The gating strategy is shown in figure S5 (d7 n=12, d14 n=9 and d30 n=7). *p=0.023, ***p=0.0003 and ****p<0.0001, Tukey's 1-way-ANOVA. **(E)** Histogram overlays of the expression of indicated markers within N2IC/hCD2^{+} MZB cells and total splenic hCD2^{-} B cells at day 7 p.i., compared to total MZB and FoB cells from unimmunized (UI) N2IC/hCD2 animals. n=9. **(F)** Chromogenic immunohistochemical analysis for the localization of hCD2^{+} cells at the indicated time

points. Splenic sections were stained for hCD2 (blue) and for basement membranes of endothelial cells lining the MZ sinus with Laminin (brown). n=3 per time point.

Generation of cells with a MZ phenotype during the primary immune response is Notch2-dependent

We next asked whether MZB cell differentiation occurs only in the transgenic setting or also physiologically in the course of TD immune responses. To answer this question, we analyzed the appearance of reporter^{+} cells with a MZB cell phenotype upon immunization of control/CAR mice. Indeed, we found reporter^{+}CD23^{low}CD21^{high} B cells in the spleen of control/CAR mice. The percentages of these cells gradually increased with ongoing time post injection (Fig. 6), ranging between 2-10% over the observation period.

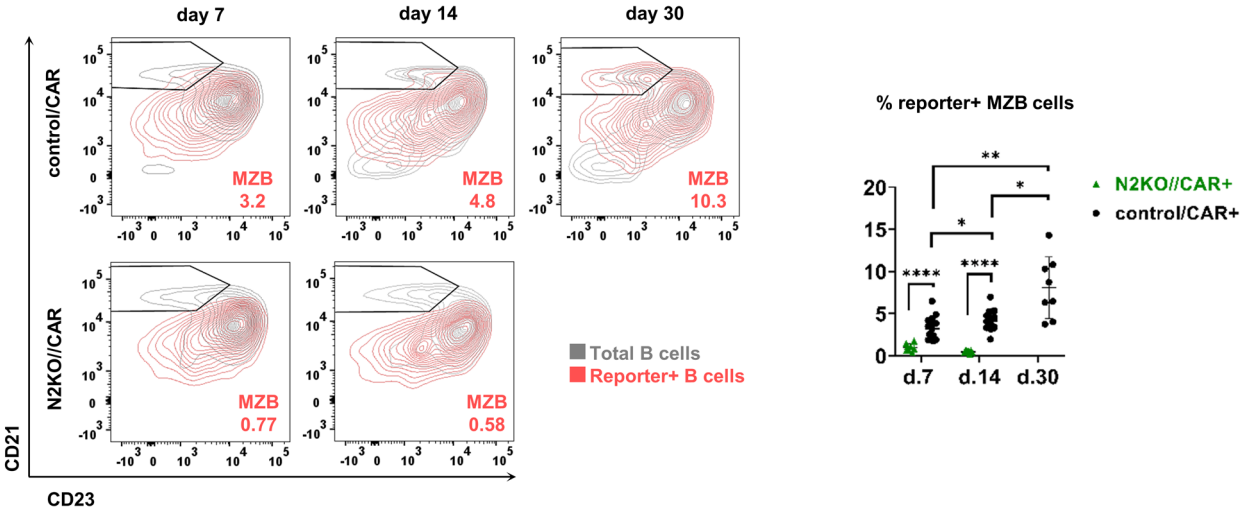

Fig. 6. Notch2 signaling is necessary for the generation of reporter^{+} cells with a MZB phenotype. Representative FACS analysis of reporter^{+}CD21^{high}CD23^{low} MZB cells overlaid with total B220^{+} B cells in control/CAR and N2KO//CAR mice. Cells are pre-gated on live lymphocytes. The graph summarizes percentages of reporter^{+} MZB cells at the indicated time points. Control/CAR mice: d7 n=16, d14 n=17, d30 n=8; N2KO//CAR mice: d7 n=8, d14 n=7. *p=0.002, **p=0.004, ****p<0.0001, Sidak's 2-way-ANOVA.

Strikingly, reporter^{+}CD23^{low}CD21^{high} B cells were significantly reduced in immunized N2KO//CAR mice compared to controls, implying that the generation of MZB cells in the course of the TD immune response is clearly Notch2-dependent (Fig. 6). In addition, the newly generated CAR^{+} MZB cells exhibited high expression of the typical MZB cell surface markers CD1d and IgM, similar to MZB cells in the bulk (Fig. S6). Taken together, our results revealed that there is a gradual generation of CAR^{+} MZB cells over a time course of 4 weeks upon TD immunization. Moreover, we could conclusively show that this process is strongly dependent on functional Notch2 signaling.

Quantitatively mapping B cell differentiation during an immune response reveals bifurcation of FoB cells into GCB and MZB cell-fates

We integrated the data from our immunization experiments into a deterministic mathematical modeling approach to quantify the dynamics of activated B cells and their diversification into MZB and GCB cell fates. We hypothesized that CAR^{+} MZB cells emerge either from activated FoB cells (branched pathway) or from GCB cells (linear pathway) (Fig. 7A), in addition to the direct activation of pre-existing MZB cells (detailed model schematics in Fig. S7A-B). We also defined a 'null model' in which all CAR^{+} MZB cells derived from the activation of MZB cells during the TD immune response (Fig. S7C), with no influx from FoB and GCB cells. The simplest forms of these branched, linear and null models assumed that both the influx of new cells into the compartment and their net loss remain unchanged over time, which we refer to as 'neutral dynamics'. We define net loss as the balance between loss by death and differentiation, and cell division. Motivated by the observed initial rapid accumulation of CAR^{+} GCB cells and the subsequent gradual decrease in their numbers (Fig. 7B), we also considered extensions to all three models that allowed for time-variation in either

the rate of recruitment of FoB cells into GCB or the rate of loss of GCB cells.

Using a Bayesian approach, we fitted each model simultaneously to the time-courses of counts of CAR^+ MZB cells, CAR^+ GCB cells and total GCB cells from control/CAR mice (red dots in Fig. 7B), assessing the relative support for each model using leave-one-out cross validation (LOO-cv). In addition, we used the data from N2KO//CAR mice (blue dots in Fig. 7B) in which B cell activation induces Notch2 deficiency and therefore prevents differentiation of CAR^+ FoB and GCB cells into a MZB phenotype. In N2KO//CAR mice, the CAR^+ fraction in the MZB subset is driven by activation of CAR^- MZB cells and self-renewal of CAR^+ MZB cells.

The branched model with time-varying influx of activated FoB cells into the GC received the strongest support from the data (table S2). This best-fitting model predicted rapid turnover of CAR^+ MZB cells (mean clonal lifespan < 2 days) (Fig. 7C) and low propensity of MZB cell activation (< 1 in 250 cells, Fig. 7E), suggesting that the CAR^+ fraction among MZB subset is largely sustained by the influx of activated FoB cells (Fig. 7F, left panel). The total influx of FoB cells into the GC compartment is estimated to be high initially (corresponding to approximately ~20% of the compartment size per day, at day 4), which then decreases sharply to near-zero by day 10 post immunization (Fig. 7G). The linear differentiation model with time-varying recruitment of FoB cells into GC showed visually similar fits (dotted lines in Fig. 7B) and comparable parameter estimates (Fig. 7C-G), as that of the best-fitting branched model, despite receiving poorer statistical support (table S2). Perhaps capturing the underlying biology of the immunization-induced MZB generation warrants a unifying model, comprising both branched and linear pathways in which CAR^+ MZB cells emerge from activated FoB cells early on and are later sustained by differentiation of GC-derived clones.

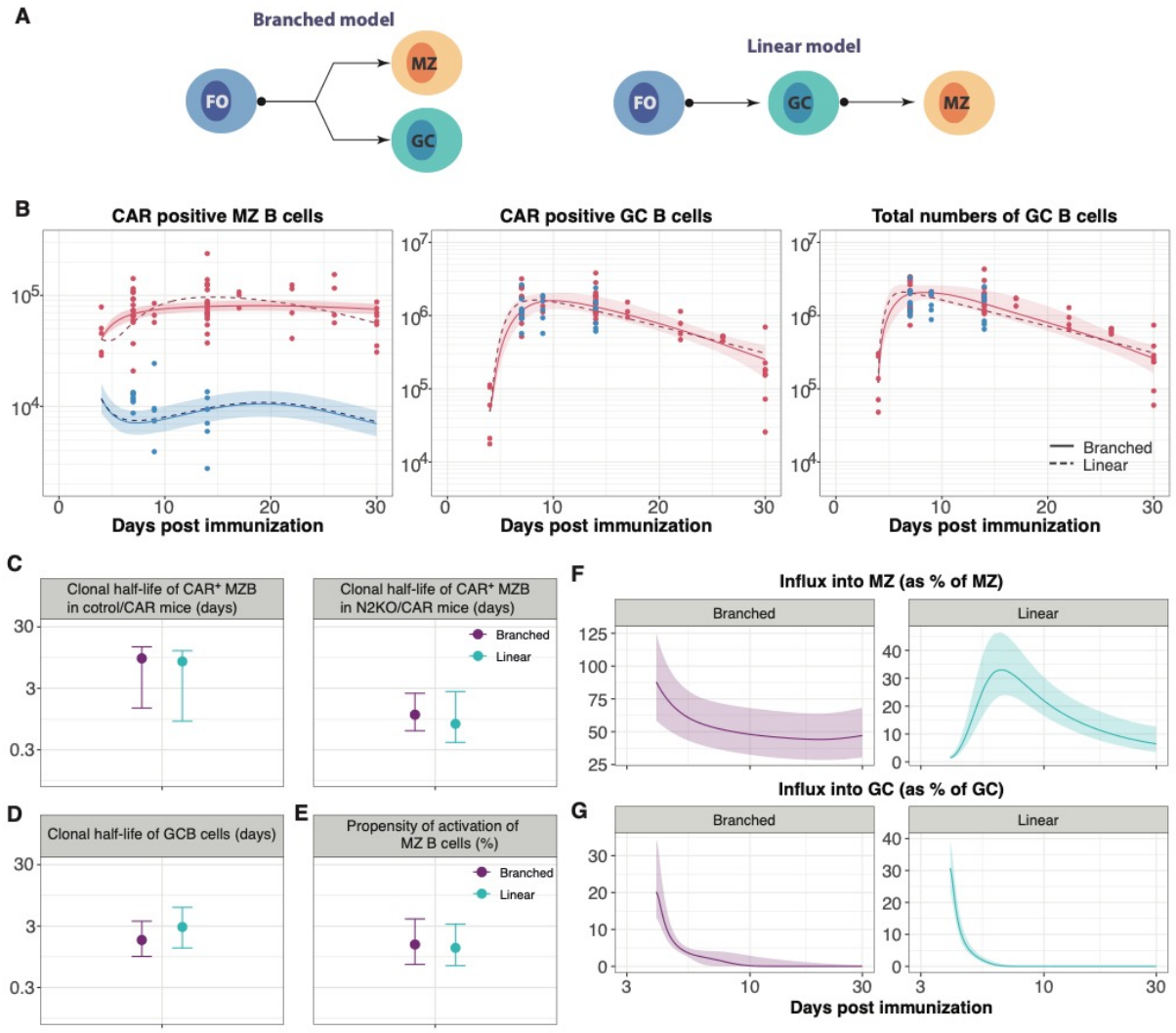

Fig. 7. Dynamics of CAR$^+$ MZB and GCB cells during a TD immune response. (A) Schematic of the models depicting B cell fate decisions during an immune response. **(B)** Time-course of counts of CAR$^+$ MZB and CAR$^+$ GCB and total GCB cells post immunization in control/CAR (red dots) and N2KO//CAR (blue dots) mice. Fits from the best-fitting branched model with time-dependence in the rate of recruitment of FoB cells into GC reactions (smooth lines) with 95% credible intervals (envelopes). We also show fits from the linear model with time-dependent recruitment (dashed lines), for visual comparison. For clarity, the envelopes around predictions from the linear model are omitted. **(C-G)** Parameter estimates from the branched (purple) and linear (cyan) models with time-dependent recruitment of FoB into GCB cells. **(C-D)** Clonal half-life is defined as the log(2)/net loss rate, which gives the time taken for the size of the clonal-lineage to change by 2-fold. **(E)** Rate of activation of CAR$^-$ MZB cells/100 cells. **(F-G)** The total daily influx of CAR$^+$ FoB cells into the MZB subset and GCB subset, plotted as % of total MZB and GC pool sizes, respectively.

Discussion

Considering the proximity to the Dll-1-expressing follicular fibroblasts, activation of Notch2 pathway in most, if not all, B cells in the splenic follicles is a possibility. How the differentiation to MZB cell-fate is regulated in B cells receiving a Notch2 signal remains unclear. We hypothesized that the Notch2 signal-strength determines whether a transitional or FoB cell ultimately develops into a MZB cell. To test this hypothesis, we analyzed the Venus expression in B cells from Notch-reporter mice. We found that both immature and mature B cells are Venus-positive, suggesting that B cells encounter Notch-ligand-expressing cells in the BM, as well as in the periphery. Venus expression gradually increased throughout stages of B cell development, reaching its highest level in MZB cells, supporting our view that strong Notch2 signaling induces MZB development. Surprisingly, a portion of MZB cells downregulated or completely lost the Venus signal, suggesting that MZB cells do not receive a *de novo* Notch signal in the MZ and therefore lose their Venus expression with time. By loss of the otherwise high Notch signal, the Venus-low MZB cells may downregulate their Sphingosine-1-phosphate-receptors (S1PR1 and S1PR3), and migrate back into the follicles (13, 25). Indeed, inhibition of Notch signaling has been shown to result in the disappearance of MZB cells (26). Alternatively, MZB cells downregulating the Notch signal could be on a path towards terminal PC-differentiation.

Earlier studies revealed that Notch2 signaling interferes with the GC reaction (14, 27), but strongly synergizes with the BCR and CD40 stimulation to enhance and sustain B-cell activation (28). These results are in line with our observation that Notch2-expression is upregulated on activated FoB cells, whereas it is progressively downregulated in GCB cells. Moreover, we found that Venus expression is strongly and progressively downregulated in GCB cells of CBF:H2B-Venus mice, indicating that Notch signaling is switched-off during the GC reaction. Instead of forming GCs, B cells receiving a strong Notch signal upon TD

immunization, adopted a CD38^{high}Bcl6^{-} non-GC phenotype. Some of these non-GC cells were Irf4^{high}B220^{low}, suggesting a PC-phenotype. However, the reporter^{+}Irf4^{high}B220^{low} cells did not reach the same high Blimp1 levels as control PCs. This suggests that Notch2IC-expression enhances plasmablast differentiation but hinders the formation of terminally differentiated mature PC. This assumption is supported by the relatively high Venus expression in plasmablasts, which is nearly abrogated in the terminally differentiated PC in CBF:H2B-Venus (Notch-reporter) mice.

Most of the reporter^{+} B cells in Notch2IC/hCD2 mice had an Irf4^{mid}B220^{+} phenotype. Approximately, one-third of these cells adopted a MZB cell surface phenotype and was localized in the MZ, indicating that TD immunization resulted in strong MZB cell differentiation in Notch2IC/hCD2 mice. Tracking the fate of reporter^{+} cells in CAR/hCD2 mice showed that also in control mice some reporter^{+} cells adopted a MZB cell phenotype after TD-immunization. This process was strongly dependent on Notch signaling, consistent with a recent publication showing that FoB to MZB transdifferentiation is dependent on Notch2 signaling (12). Earlier studies hinted at the antigen-dependent generation of MZB cells (29-33) and clonally related FoB and MZB cells were identified in rats (34). However, it remained unclear whether these MZB cells originate from GC or pre-GC stages. Our mathematical modeling analyses and data from Notch2IC/hCD2 and N2KO//CAR mice favored a Notch2-dependent pathway, in which MZB cells branch out from activated B cells prior to differentiation into the GC stage. We did not explore a more general model in which both pre-GC and GCB cells differentiate into MZB cells, which remains a strong possibility. In this scenario, the CAR^{+} MZB compartment would be a mixture of memory B cells with somatically mutated Igs on their surface and non-mutated, IgM-expressing 'antigen-experienced' cells. This heterogeneity would be apparent in the BCR repertoire of the CAR-expressing MZB cells generated upon immunization. These results suggest that self-antigen induced B cell activation

may also contribute to the steady-state development of MZB cells, which explains the presence of CAR^+ MZB cells in control/CAR mice prior to immunization (day 0) and provides a rationale for the generation of the MZB-derived 'natural antibody' reservoir (3, 35).

Our best-fit model (branched pathway with time-dependent influx into GC) predicts that CAR-expressing MZB cells have a short residence time (<2 days), and are largely maintained by the influx from activated FoB cells. Considering that CAR^+ MZB cells are generated because they received a strong Notch signal in combination with a BCR+CD40 signal, it is likely that they upregulate c-myc and mTOR signaling (36, 37) both of which are described to induce rapid division-independent PC-differentiation of MZB cells (38, 39). This differentiation into PCs may be responsible for the rapid loss of CAR^+ cells from the MZB compartment. Earlier studies found antigen-specific memory B cells to be equally distributed between the MZ and B cell follicles, even 8 weeks after immunization (40). Understanding whether post-GC memory cells would support long-term maintenance of CAR^+ MZB cells warrants further investigation. Mapping the clonal relationship between antigen-induced memory B cells and MZB cells may help to further clarify this issue.

Previous studies of GC dynamics mainly focused on modeling the affinity maturation processes (41, 42), while the processes driving their generation and maintenance remain relatively unexplored (43). Clonal linages in the GCs have been shown to persist for over 3-4 weeks by rapid division and turnover of their constituents, at steady-states in unimmunized mice (44). Here, we estimate that B cell clones reside in GCs for relatively shorter duration (~9 days) after TD-immunization. In addition, our analysis showed that influx into GC varies with time post-immunization (fraction of newly-recruited FoB cells falls from ~20% at day 4 to near-zero by day 10, Fig. 7G). We speculate that the initial transient rise in GCB cells is largely driven by the rapid influx of FoB cells, while the maintenance of their pool size after a week post-

immunization is governed by the expansion and contraction of 'founder-clones' that are established during the first week of the response, which agrees with previous findings (45, 46).

Findings from this study suggest that the human and murine MZB cell compartment may be more similar than previously suspected. Human´s MZB cell compartment is heterogeneous and its clonal composition appears to change with age (47, 48). In children under the age of two, majority of MZB cells carry unique BCRs with low mutation frequencies. In contrast, in older children and adults, MZB cells display clonal relationships and are hypermutated, suggesting that naïve MZB cells are progressively replaced by antigen-experienced cells (47). It will be interesting to explore whether the clonal composition and frequencies of hypermutated MZB cells change during aging of mice and whether the ratio of naïve and antigen-experienced MZB cells can be shifted in favor of antigen-experienced MZB cells by frequent antigenic exposures.

Materials and Methods

Study Design

The objective of this study was to elucidate MZB cell differentiation in mice upon TD-immunization. To examine which B cells receive a Notch signal in the steady state and upon immunization, we analyzed the Venus expression in different B cell populations from CBF:H2B-Venus (Notch-reporter) mice. By using conditional Notch2IC-KI and Notch2-KO mice in combination with the GC-specific strain Cγ1-Cre, we followed the fate of transgenic antigen-responding B cells with enhanced or reduced Notch signaling in comparison to controls by flow cytometry and immunohistochemistry. In addition, we developed an array of dynamical mathematical models to define and quantify the generation and maintenance MZB and GC cells during an active immune response. Throughout the study, control and mutant mice were age-matched and examined in parallel. Analyses were performed in female and male

mice in an unblinded way. All mouse strains were on Balb/c background and analyzed at 10 to 18 weeks of age. Samples sizes and statistical analyses are indicated in figure legends.

Antibodies used in this study.

The different antibodies used in FACS, ELISA/ELISpot and histology are listed in Table S1.

Mice

CBF:H2B-Venus reporter mice (22) were purchased from The Jackson Laboratory, backcrossed into the Balb/c background and further maintained in house. Previously described R26/CAG-CARΔ1^{StopF} (24) and N2IC^{flSTOP} mice (14) were crossbred to the Cγ1-Cre strain (23) to generate R26/CAG-CARΔ1^{StopF}//γ1-Cre (control/CAR) and N2IC^{flSTOP}//γ1-Cre mice (N2IC/hCD2), respectively. Notch2$^{fl/fl}$ mice (17) were mated to the R26/CAG-CARΔ1^{StopF}//γ1-Cre animals to obtain the Notch2$^{fl/fl}$//R26/CAG-CARΔ1^{StopF}//Cγ1-Cre (N2KO//CAR) mice. Animals were maintained in specific pathogen-free conditions. Experiments were performed in compliance with the German Animal Welfare Law and were approved by the Institutional Committee on Animal Experimentation and the Government of Upper Bavaria.

Mouse immunizations

To trigger TD immune responses, 10- to 18- week-old mice were injected intraperitoneally with 100 µg of alum-precipitated 4-hydroxy-3-nitrophenylacetyl (NP)-chicken-gamma-globulin (CCG) (Biosearch Technologies, Novato, CA) in 200 µl sterile PBS (Gibco).

Cell purification and *in vitro* cultures

Naïve FoB cells of wildtype Balb/c mice were purified from splenic cell suspension using the MZB and FoB Cell Isolation Kit (Miltenyi Biotech) according to the manufacturer's instructions. Cells were cultured for up to 72 h at a density of 5×10^5 cells/ml in flat-bottom 96-well plates in RPMI-1640 medium (Gibco), supplemented with 10% fetal calf serum (FCS,

PAA Cell Culture Company), 1% L-glutamine, 1% non-essential amino acids, 1% sodium pyruvate and 50 μM β-mercaptoethanol. With the exception of FCS, all supplements were purchased from Gibco. An agonistic antibody against CD40 (2.5 μg/ml; eBioscience HM40-3) and an antibody specific for IgM (15 μg/ml; AffiniPure F(ab′)2 goat anti-mouse IgM, μ-chain, Dianova) was used as a combined stimulus.

Histology

Murine splenic tissues were embedded in O.C.T. compound (VWR Chemicals, USA), snap frozen and stored at −20 °C. Tissues were sliced with a cryostat with 7 μm thickness, mounted on glass slides and stored at −80 °C for immunohistochemical (IHC) analysis. Chromogenic IHC and immunofluorescence (IF) was performed as described by (13, 49). IHC microscopy slides were analyzed using an Axioscope (Zeiss) microscope, equipped with an AxioCam MRc5 digital camera (Carl Zeiss GmbH). IF images were acquired on a TCS SP5 II confocal microscope (Leica) and picture stacks were composed in ImageJ.

ELISA and ELISpot

NP-specific antibody titers in the sera were measured by ELISA, following the procedure described by (49). The absorbance was determined with a microplate ELISA reader (Photometer Sunrise RC, Tecan) at an optical density (OD) at 405 nm. All NP-specific titers are given as log10 relative units. For antigen-specific ELISpot with splenic or BM cells, 96-well ELISpot plates (Millipore) were coated overnight at 4°C with NP3– or NP14–bovine serum albumin (BSA; Biosearch Technologies). Subsequent analyses were performed as previously described (51). Spots were visualized and counted with the ImmunoSpot Series 5 UV Analyzer (CTL Europe).

Flow cytometry (FACS)

Surface staining of lymphocytes was performed on ice for 25 min in MACS buffer (Miltenyi). To omit dead cells from the analysis, cells were stained either with TO-PRO-3 (Molecular Probes) for 5 min on ice prior acquisition, or for 20 min on ice with LIVE/DEAD Fixable Blue Dead Cell Stain Kit (Invitrogen) before the surface antibody staining. For intracellular FACS staining, cells were fixed with 2% paraformaldehyde (1:2 PBS-diluted Histofix) for 10 min at room temperature and permeabilized in ice-cold 100% methanol for 10 min on ice. Cells were incubated for 1 h at room temperature with the corresponding antibodies. Dead cells were excluded by staining for 5 min on ice with LIVE/DEAD Fixable Blue Dead Cell Stain Kit (Invitrogen) before fixation. Cytometry analysis was performed on a LSRII FACS Fortessa (BD Biosciences). Results were evaluated using FlowJo (v9 and v10).

Statistics

All statistical analyses, including testing for distributions and equal variance, calculations of means and SDs, determining p-values of 1-way or 2-way ANOVA with multiple comparisons tests were done with GraphPad Prism (versions 8 through 10). P values of less than 0.05 were considered significant. *$P < 0.05$, **$P < 0.01$, ***$P < 0.001$, and ****$P < 0.0001$. Error bars in all figures define means ± SD. The Prism software was also used to generate all statistical plots.

Mathematical modeling and statistical analysis

We developed an array of dynamical mathematical models (details in Text S1) and fitted them to the counts of CAR^+ MZB, CAR^+ GCB, and total GCB cells in control/CAR (WT) and N2KO//CAR mice. We used the empirical descriptions of the pool sizes of CAR^+ FoB cells and CAR^- MZB cells to define the influx into CAR^+ MZB and CAR^+ GC compartments (details in Text S2). Models were validated using the Bayesian statistical approach in the programming language *Stan* and predictions were analyzed and plotted in *R*. Leave-One-Out

(LOO) cross validation method was used to compare and rank the models (details in Text S3). Code and data used to perform model fitting are freely available at this linked Github repository.

Supplementary Materials:

Fig. S1. Venus expression in the LZ and DZ of splenic GCB cells.

Fig. S2. Mouse models for GCB-cell-specific inactivation or constitutive activation of Notch2.

Fig. S3. Notch2 surface expression on FoB cells after *in vitro* stimulation and on CAR^+ CD38/CD95 subpopulations after TD immunization *in vivo*.

Fig. S4. NP-specific serum titers and NP-specific PCs in the spleen and BM

Fig. S5. CD23/CD21 staining to separate and quantify MZB cells in N2IC/hCD2 mice.

Fig. S6. IgM and CD1d surface phenotyping of CAR^+ CD23/CD21 subpopulations of control/CAR animals.

Fig. S7. Detailed schematics of the 3 main models with pathways of $reporter^+$ MZB cell generation.

Fig. S8. Empirical descriptions of the dynamics of the numbers of FoB and MZB cells.

Table S1. List of antibodies used in this study.

Table S2. Comparison of models describing population dynamics of MZB and GCB cell populations upon TD immunization.

Text S1. Mathematical models of B cell dynamics during a TD immune response.

Text S2. Defining phenomenological functions to capture the dynamics of precursor populations for the GC and CAR-expressing MZB cells.

Text S3. Model ranking and selection criteria.

Acknowledgements: We thank the animal facility of the Helmholtz Center for the excellent housing of the mice and Krisztina Zeller for exquisite technical help. **Funding:** This work was supported by the Deutsche Forschungsgemeinschaft (DFG ZI1382/4-1). **Authorship Contributions:** T.B. designed, performed and analyzed most experiments. S.R. developed and performed mathematical modeling and contributed to manuscript writing. M.L. performed experiments. A.J.Y. contributed to mathematical modeling and manuscript editing. L.J.S and U.Z.-S contributed to experimental design, data interpretation and manuscript preparation. T.B. and U.Z.-S. wrote the manuscript. All authors read and approved the final version. **Competing interest:** The authors declare no competing interest.

References

1. Arnon TI, Horton RM, Grigorova IL, Cyster JG. Visualization of splenic marginal zone B-cell shuttling and follicular B-cell egress. Nature. 2013;493(7434):684-8.
2. Martin F, Oliver AM, Kearney JF. Marginal zone and B1 B cells unite in the early response against T-independent blood-borne particulate antigens. Immunity. 2001;14(5):617-29.
3. Cerutti A, Cols M, Puga I. Marginal zone B cells: virtues of innate-like antibody-producing lymphocytes. Nat Rev Immunol. 2013;13(2):118-32.
4. Shlomchik MJ, Luo W, Weisel F. Linking signaling and selection in the germinal center. Immunol Rev. 2019;288(1):49-63.
5. Pillai S, Cariappa A. The follicular versus marginal zone B lymphocyte cell fate decision. Nat Rev Immunol. 2009;9(11):767-77.
6. Allman D, Lindsley RC, DeMuth W, Rudd K, Shinton SA, Hardy RR. Resolution of three nonproliferative immature splenic B cell subsets reveals multiple selection points during peripheral B cell maturation. J Immunol. 2001;167(12):6834-40.
7. Martin F, Kearney JF. Positive selection from newly formed to marginal zone B cells depends on the rate of clonal production, CD19, and btk. Immunity. 2000;12(1):39-49.
8. Srivastava B, Quinn WJ, 3rd, Hazard K, Erikson J, Allman D. Characterization of marginal zone B cell precursors. J Exp Med. 2005;202(9):1225-34.

9. Vinuesa CG, Sze DM, Cook MC, Toellner KM, Klaus GG, Ball J, et al. Recirculating and germinal center B cells differentiate into cells responsive to polysaccharide antigens. Eur J Immunol. 2003;33(2):297-305.
10. Agenes F, Freitas AA. Transfer of small resting B cells into immunodeficient hosts results in the selection of a self-renewing activated B cell population. J Exp Med. 1999;189(2):319-30.
11. Cariappa A, Boboila C, Moran ST, Liu H, Shi HN, Pillai S. The recirculating B cell pool contains two functionally distinct, long-lived, posttransitional, follicular B cell populations. J Immunol. 2007;179(4):2270-81.
12. Gomez Atria D, Gaudette BT, Londregan J, Kelly S, Perkey E, Allman A, et al. Stromal Notch ligands foster lymphopenia-driven functional plasticity and homeostatic proliferation of naive B cells. J Clin Invest. 2022.
13. Lechner M, Engleitner T, Babushku T, Schmidt-Supprian M, Rad R, Strobl LJ, et al. Notch2-mediated plasticity between marginal zone and follicular B cells. Nat Commun. 2021;12(1):1111.
14. Hampel F, Ehrenberg S, Hojer C, Draeseke A, Marschall-Schroter G, Kuhn R, et al. CD19-independent instruction of murine marginal zone B-cell development by constitutive Notch2 signaling. Blood. 2011;118(24):6321-31.
15. Saito T, Chiba S, Ichikawa M, Kunisato A, Asai T, Shimizu K, et al. Notch2 is preferentially expressed in mature B cells and indispensable for marginal zone B lineage development. Immunity. 2003;18(5):675-85.
16. Hozumi K, Negishi N, Suzuki D, Abe N, Sotomaru Y, Tamaoki N, et al. Delta-like 1 is necessary for the generation of marginal zone B cells but not T cells in vivo. Nat Immunol. 2004;5(6):638-44.
17. Besseyrias V, Fiorini E, Strobl LJ, Zimber-Strobl U, Dumortier A, Koch U, et al. Hierarchy of Notch-Delta interactions promoting T cell lineage commitment and maturation. J Exp Med. 2007;204(2):331-43.
18. Tan JB, Xu K, Cretegny K, Visan I, Yuan JS, Egan SE, et al. Lunatic and manic fringe cooperatively enhance marginal zone B cell precursor competition for delta-like 1 in splenic endothelial niches. Immunity. 2009;30(2):254-63.
19. Fasnacht N, Huang HY, Koch U, Favre S, Auderset F, Chai Q, et al. Specific fibroblastic niches in secondary lymphoid organs orchestrate distinct Notch-regulated immune responses. J Exp Med. 2014;211(11):2265-79.
20. Lopes-Carvalho T, Kearney JF. Development and selection of marginal zone B cells. Immunol Rev. 2004;197:192-205.
21. Hammad H, Vanderkerken M, Pouliot P, Deswarte K, Toussaint W, Vergote K, et al. Transitional B cells commit to marginal zone B cell fate by Taok3-mediated surface expression of ADAM10. Nat Immunol. 2017;18(3):313-20.
22. Nowotschin S, Xenopoulos P, Schrode N, Hadjantonakis AK. A bright single-cell resolution live imaging reporter of Notch signaling in the mouse. BMC Dev Biol. 2013;13:15.
23. Casola S, Cattoretti G, Uyttersprot N, Koralov SB, Seagal J, Hao Z, et al. Tracking germinal center B cells expressing germ-line immunoglobulin gamma1 transcripts by conditional gene targeting. Proc Natl Acad Sci U S A. 2006;103(19):7396-401.
24. Heger K, Kober M, Riess D, Drees C, de Vries I, Bertossi A, et al. A novel Cre recombinase reporter mouse strain facilitates selective and efficient infection of primary immune cells with adenoviral vectors. Eur J Immunol. 2015;45(6):1614-20.
25. Cinamon G, Zachariah MA, Lam OM, Foss FW, Jr., Cyster JG. Follicular shuttling of marginal zone B cells facilitates antigen transport. Nat Immunol. 2008;9(1):54-62.
26. Simonetti G, Carette A, Silva K, Wang H, De Silva NS, Heise N, et al. IRF4 controls the positioning of mature B cells in the lymphoid microenvironments by regulating NOTCH2 expression and activity. J Exp Med. 2013;210(13):2887-902.
27. Valls E, Lobry C, Geng H, Wang L, Cardenas M, Rivas M, et al. BCL6 Antagonizes NOTCH2 to Maintain Survival of Human Follicular Lymphoma Cells. Cancer Discov. 2017;7(5):506-21.

28. Thomas M, Calamito M, Srivastava B, Maillard I, Pear WS, Allman D. Notch activity synergizes with B-cell-receptor and CD40 signaling to enhance B-cell activation. Blood. 2007;109(8):3342-50.
29. Liu YJ, Oldfield S, MacLennan IC. Memory B cells in T cell-dependent antibody responses colonize the splenic marginal zones. Eur J Immunol. 1988;18(3):355-62.
30. Shih TA, Roederer M, Nussenzweig MC. Role of antigen receptor affinity in T cell-independent antibody responses in vivo. Nat Immunol. 2002;3(4):399-406.
31. Obukhanych TV, Nussenzweig MC. T-independent type II immune responses generate memory B cells. J Exp Med. 2006;203(2):305-10.
32. Pape KA, Kouskoff V, Nemazee D, Tang HL, Cyster JG, Tze LE, et al. Visualization of the genesis and fate of isotype-switched B cells during a primary immune response. J Exp Med. 2003;197(12):1677-87.
33. White HN, Meng QH. Recruitment of a distinct but related set of VH sequences into the murine CD21hi/CD23- marginal zone B cell repertoire to that seen in the class-switched antibody response. J Immunol. 2012;188(1):287-93.
34. Hendricks J, Visser A, Dammers PM, Burgerhof JGM, Bos NA, Kroese FGM. The formation of mutated IgM memory B cells in rat splenic marginal zones is an antigen dependent process. PLoS One. 2019;14(9):e0220933.
35. Wen L, Brill-Dashoff J, Shinton SA, Asano M, Hardy RR, Hayakawa K. Evidence of marginal-zone B cell-positive selection in spleen. Immunity. 2005;23(3):297-308.
36. Weng AP, Millholland JM, Yashiro-Ohtani Y, Arcangeli ML, Lau A, Wai C, et al. c-Myc is an important direct target of Notch1 in T-cell acute lymphoblastic leukemia/lymphoma. Genes Dev. 2006;20(15):2096-109.
37. Chan SM, Weng AP, Tibshirani R, Aster JC, Utz PJ. Notch signals positively regulate activity of the mTOR pathway in T-cell acute lymphoblastic leukemia. Blood. 2007;110(1):278-86.
38. Gaudette BT, Roman CJ, Ochoa TA, Gomez Atria D, Jones DD, Siebel CW, et al. Resting innate-like B cells leverage sustained Notch2/mTORC1 signaling to achieve rapid and mitosis-independent plasma cell differentiation. J Clin Invest. 2021;131(20).
39. Limon JJ, Fruman DA. Akt and mTOR in B Cell Activation and Differentiation. Front Immunol. 2012;3:228.
40. Anderson SM, Tomayko MM, Ahuja A, Haberman AM, Shlomchik MJ. New markers for murine memory B cells that define mutated and unmutated subsets. J Exp Med. 2007;204(9):2103-14.
41. Zhang J, Shakhnovich EI. Optimality of mutation and selection in germinal centers. PLoS Comput Biol. 2010;6(6):e1000800.
42. Amitai A, Mesin L, Victora GD, Kardar M, Chakraborty AK. A Population Dynamics Model for Clonal Diversity in a Germinal Center. Front Microbiol. 2017;8:1693.
43. Faro J, von Haeften B, Gardner R, Faro E. A Sensitivity Analysis Comparison of Three Models for the Dynamics of Germinal Centers. Front Immunol. 2019;10:2038.
44. Verheijen M, Rane S, Pearson C, Yates AJ, Seddon B. Fate Mapping Quantifies the Dynamics of B Cell Development and Activation throughout Life. Cell Rep. 2020;33(7):108376.
45. Meyer-Hermann M, Binder SC, Mesin L, Victora GD. Computer Simulation of Multi-Color Brainbow Staining and Clonal Evolution of B Cells in Germinal Centers. Front Immunol. 2018;9:2020.
46. Tas JM, Mesin L, Pasqual G, Targ S, Jacobsen JT, Mano YM, et al. Visualizing antibody affinity maturation in germinal centers. Science. 2016;351(6277):1048-54.
47. Kibler A, Budeus B, Homp E, Bronischewski K, Berg V, Sellmann L, et al. Systematic memory B cell archiving and random display shape the human splenic marginal zone throughout life. J Exp Med. 2021;218(4).
48. Siu JHY, Pitcher MJ, Tull TJ, Velounias RL, Guesdon W, Montorsi L, et al. Two subsets of human marginal zone B cells resolved by global analysis of lymphoid tissues and blood. Sci Immunol. 2022;7(69):eabm9060.

49. Sperling SA, Fiedler P, Lechner M, Pollithy A, Ehrenberg S, Schiefer AI, et al. Chronic CD30-signaling in B cells results in lymphomagenesis by driving the expansion of plasmablasts and B1 cells. Blood. 2019.

Supplementary Figures and Legends

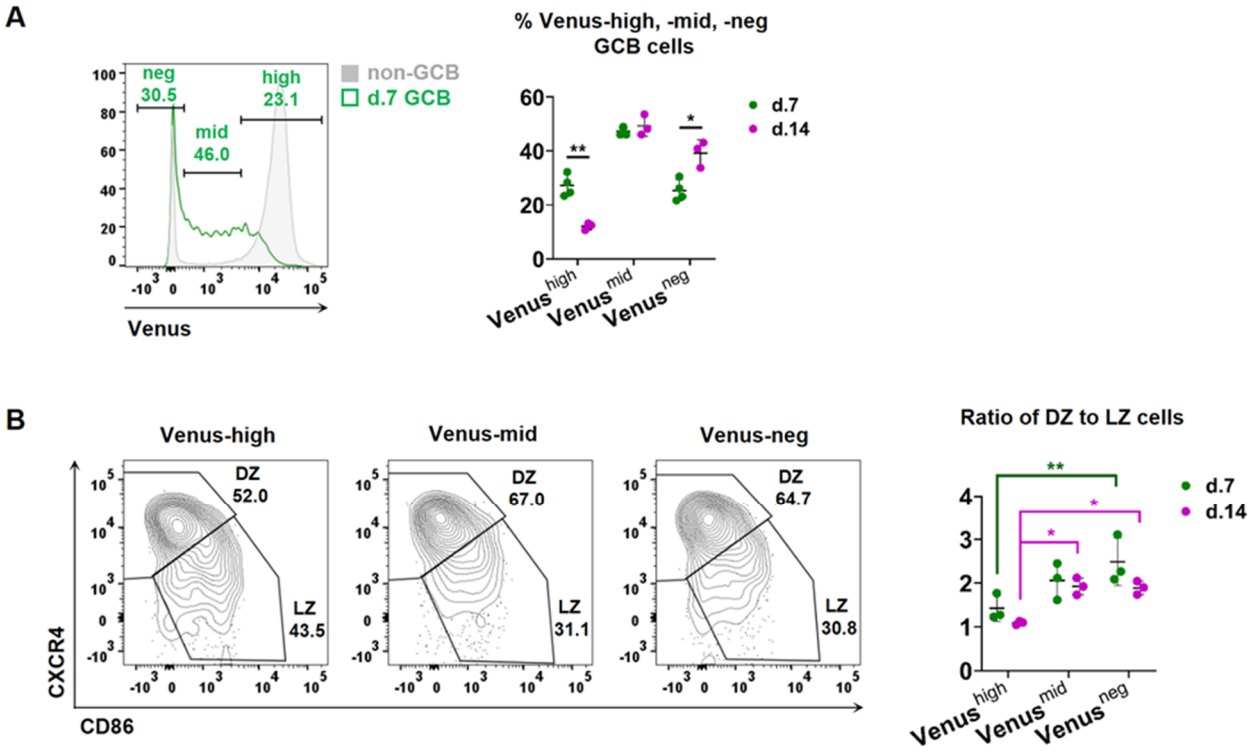

Fig. S1. Venus expression in the LZ and DZ of splenic GCB cells. (A) The histogram shows the overlay of Venus expression in GCB and non-GCB cells at day 7 p.i.. GCB cells ($CD95^{+}CD38^{low}$) were divided into 3 subpopulations according to their Venus-expression: $Venus^{neg}$, $Venus^{mid}$ and $Venus^{high}$. The graph depicts the percentages of the 3 subpopulations at indicated time points. **p=0.007 and *p=0.049, 2-way-ANOVA, Sidak's multiple comparisons test. d7 n=4, d14 n=3. **(B)** The $Venus^{high}$, $Venus^{mid}$, and $Venus^{low}$ GCB cells were analyzed for their DZ ($CXCR4^{high}CD86^{low}$) and LZ ($CXCR4^{low}CD86^{high}$) distribution. FACS plots are representative for day 7 p.i.. The graph depicts the ratio of the percentages of DZ to LZ cells for the 3 Venus subpopulations. A lower DZ to LZ ratio suggests an enrichment of the indicated Venus subpopulation in the LZ. **p=0.004 and *p ≤ 0.030, 2-way-ANOVA, Sidak's multiple comparisons test. n=3.

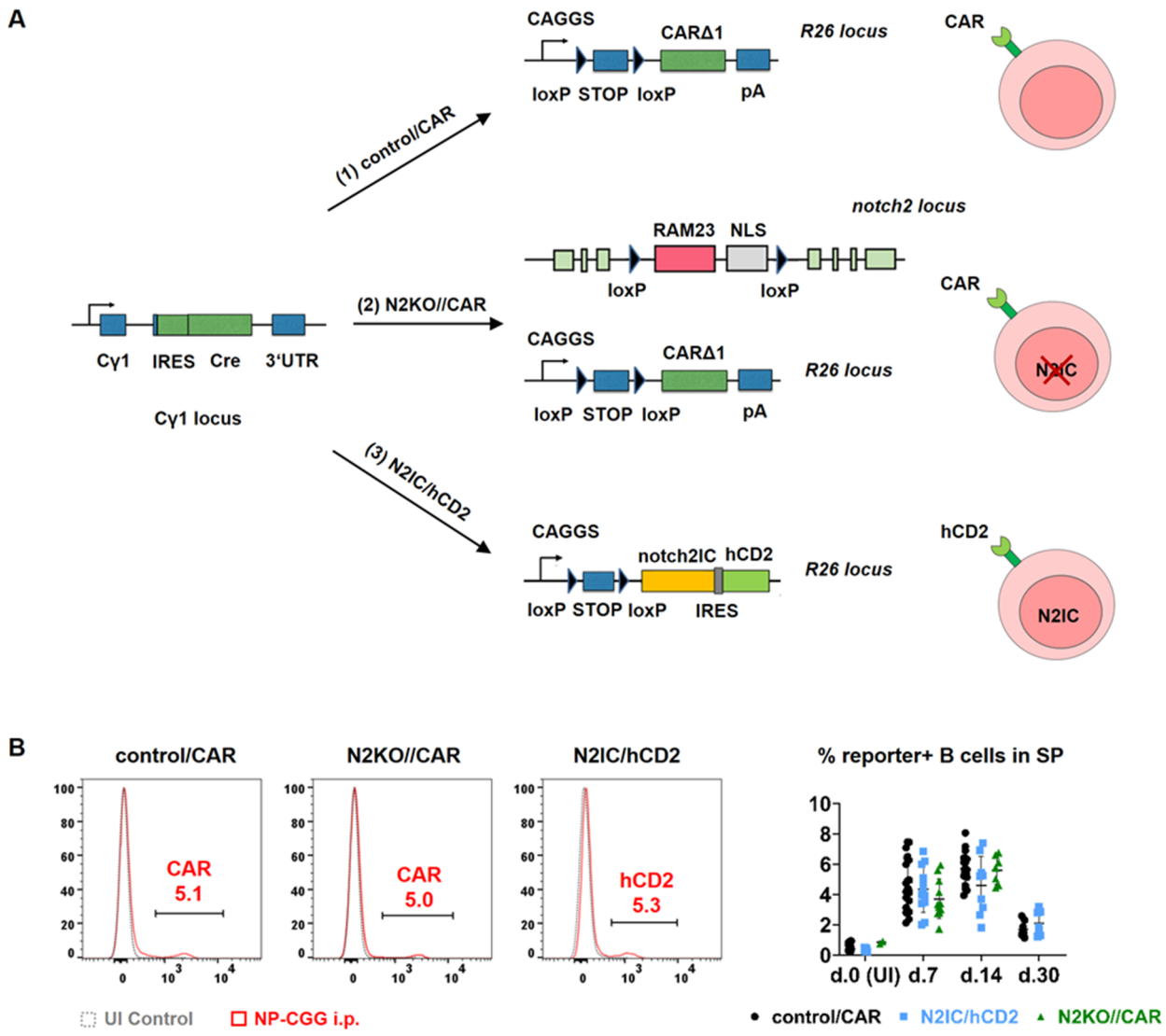

Fig. S2. Mouse models for GCB-cell-specific inactivation or constitutive activation of Notch2. (A) To ablate or induce Notch2 in GCB cells, conditional Notch2$^{fl/fl}$ (Besseyrias et al., *JEM* 2007) or Notch2IC^{stopfl} (Hampel et al., *Blood* 2011) mice were crossed with the Cγ1-Cre strain (Casola et al., *PNAS* 2006). As controls, we used the reporter mice R26-CARΔ1^{stopF} (Heger et al., *Eur. J. Immunol.* 2015), which contain the coding sequence for the coxsackie/adenovirus receptor (CAR) in the *rosa26* locus. (1) Control/CAR: Cre recombinase activity leads to deletion of the stop-cassette upstream of the *carΔ1* transgene, resulting in expression of a truncated version of CAR on the cell surface. (2) N2KO//CAR: To detect cells, which deleted the Notch2-allele, we combined Notch2$^{fl/fl}$ mice with the reporter control/CAR strain. In the *notch2* locus, exons coding for the intracellular RAM23 domain and nuclear localization signal are flanked with loxP sites. Upon Cre-mediated recombination, both the floxed *notch2* exons and the stop-cassette upstream of *carΔ1* are excised, resulting in the inactivation of Notch2 (N2KO) and expression of CAR on the cell surface. (3) N2IC/hCD2: the coding sequence for *notch2IC* is inserted into the *rosa26* locus. An IRES element and the transgene *hcd2* coding for a

truncated version of the human CD2 receptor are inserted downstream of the *notch2IC*. Cre-mediated excision results in expression of Notch2IC inside the cell and hCD2 on the cell surface. **(B)** Determination of reporter gene expression by FACS analyses of splenic B lymphocytes after immunization with 100 µg NP-CGG. Histograms are pre-gated on live $B220^+$ lymphocytes**.** Percentages of $reporter^+$ $B220^+$ cells at indicated time points are summarized in the graph. d0 n≥2, d7 n≥11, d14 n≥7, d30 n≥7. UI = unimmunized mouse; NP-CGG i.p. = intraperitoneal NP-CGG injection.

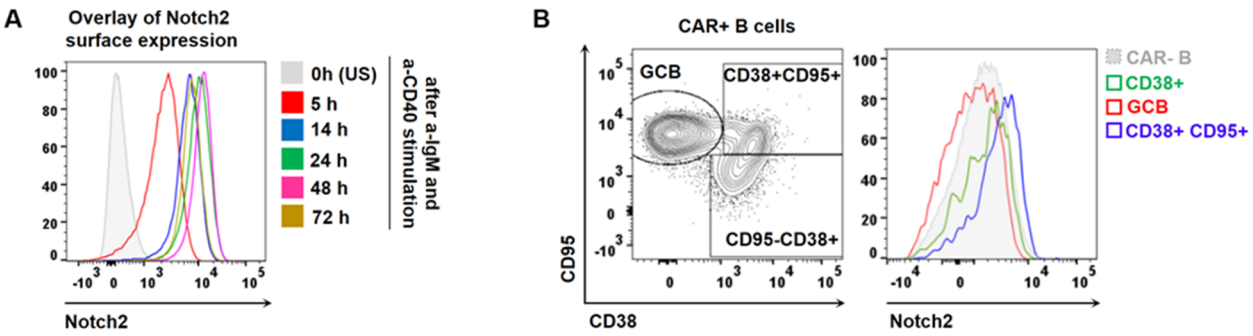

Fig. S3. Notch2 surface expression on FoB cells after *in vitro* stimulation and on CAR$^+$ CD38/CD95 subpopulations after TD immunization *in vivo*. (A) An exemplary FACS overlay from one mouse, depicting the Notch2 receptor expression on the cell surface of isolated FoB cells at indicated time points after *in vitro* stimulation with anti-CD40 and anti-IgM. **(B)** Representative FACS analysis of the gating strategy for CAR$^+$ CD38/CD95 B cell populations and a histogram overlay of the Notch2 cell surface expression on the indicated cell subpopulations at day 14 p.i..

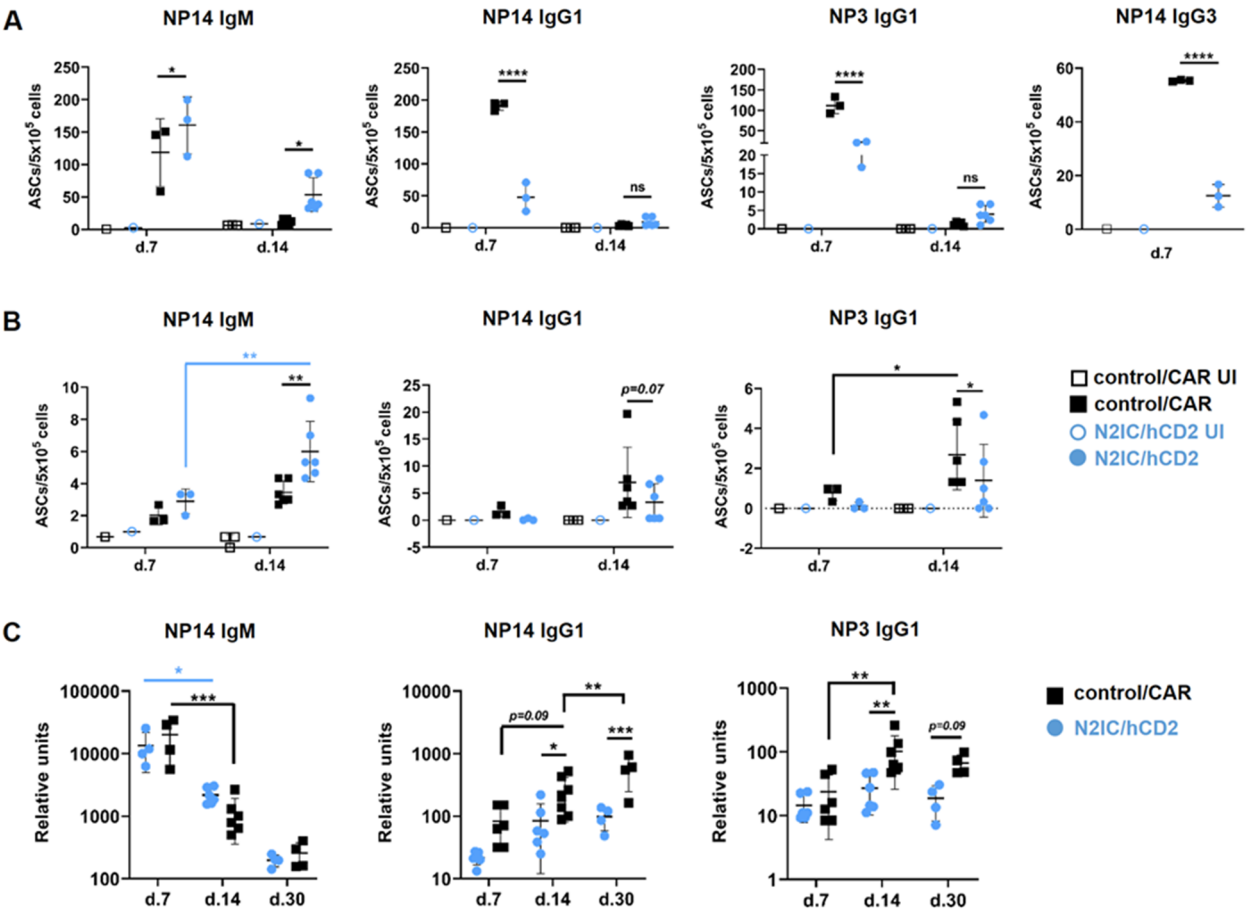

Fig. S4. NP-specific serum titers and NP-specific ASCs in the spleen and BM. (A and B) Total (binding to NP14-BSA) and high affinity (binding to NP3-BSA) antibody-secreting cells (ASCs) of the indicated isotypes were determined in the spleen (A) and BM (B) of mice at days 7 and 14 p.i. by ELISpot analyses. n≤3. *p=0.05 **p=0.006 and ****p<0.0001, 2-way-ANOVA, Sidak's multiple comparisons test. **(C)** Titers of total (NP14) and high affinity (NP3) NP-specific antibodies of the indicated isotypes were measured by ELISA in the serum of N2IC/hCD2 and control/CAR mice at the indicated time points p.i. n≥4. *p ≤ 0.049, **p=0.003 and ***p=0.0002, 2-way-ANOVA, Tukey's (NP14-IgM) and Sidak's (NP14-IgG1, NP3-IgG1) multiple comparisons test. UI = unimmunized mouse; p.i = post immunization.

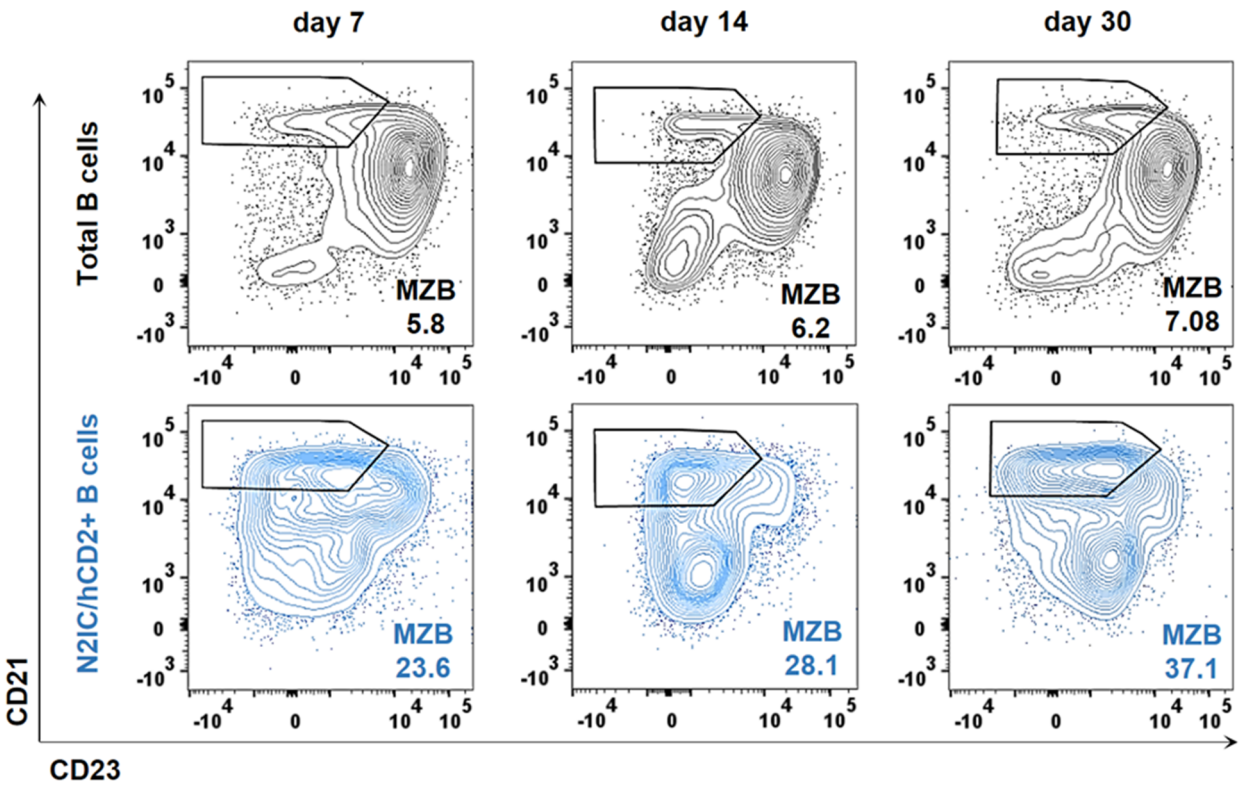

Fig. S5. CD23/CD21 staining to separate and quantify MZB cells in N2IC/hCD2 mice. Representative FACS plots of the separation of CD21^{high}CD23^{low} MZB cells among total mature B220^{+} B cells (upper row, black) and reporter^{+} B cells (lower row, blue) in N2IC/hCD2 mice at the indicated time points post immunization (p.i.).

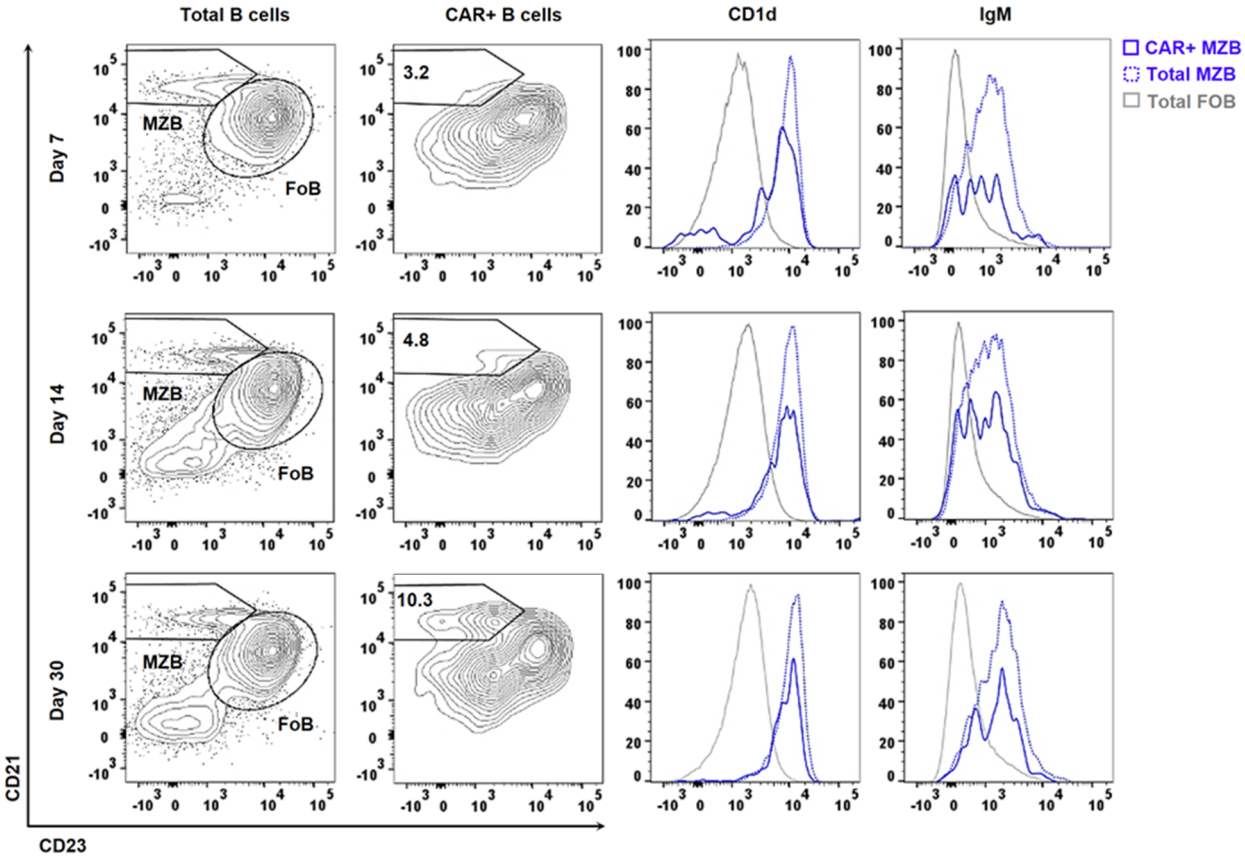

Fig. S6. IgM and CD1d surface phenotyping of CAR^{+} CD23/CD21 subpopulations of control/CAR animals. Exemplary FACS plots to illustrate the gating of total MZB cells (CD23^{low}CD21^{high}), total FoB cells and newly generated MZB cells (CAR^{+}CD23^{low}CD21^{high}). The histogram overlays show cell surface expression levels of CD1d and IgM on the gated CAR^{+} MZB population (blue, solid), compared to the total MZB (blue, dotted) and total FoB cells (grey, solid) in control/CAR mice at indicated time points post TD-immunization with NP-CGG (p.i.).

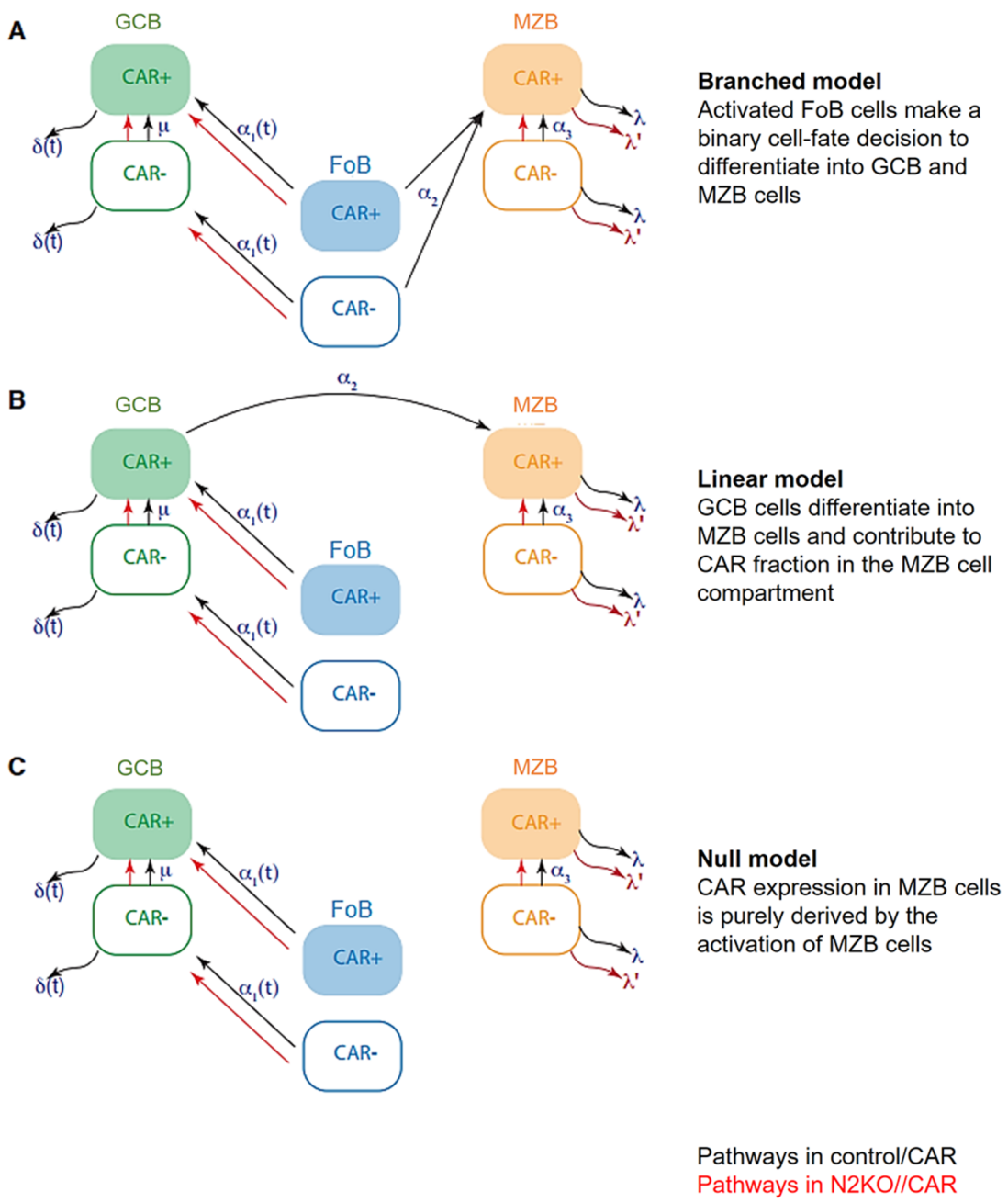

Fig. S7. Detailed schematics of the 3 main models with pathways of reporter$^+$ MZB cell generation. (A) Branched model: CAR$^+$ MZB cells emerge from activated FoB cells in a GC-independent manner. **(B)** Linear model: CAR$^+$ MZB cells arise from CAR$^+$ cells, which have undergone GC reactions first. **(C)** Null model: CAR$^+$ MZB cells are purely derived by activation of the existing, non-transgenic CAR$^-$ MZB cells. **(A-C)** Red arrows depict pathways of differentiation in N2KO//CAR mice and black arrows the differentiation processes in control/CAR (WT) mice. α_1, α_2 and α_3 are *per capita* rates of differentiation for the respective precursor cell populations in each model.

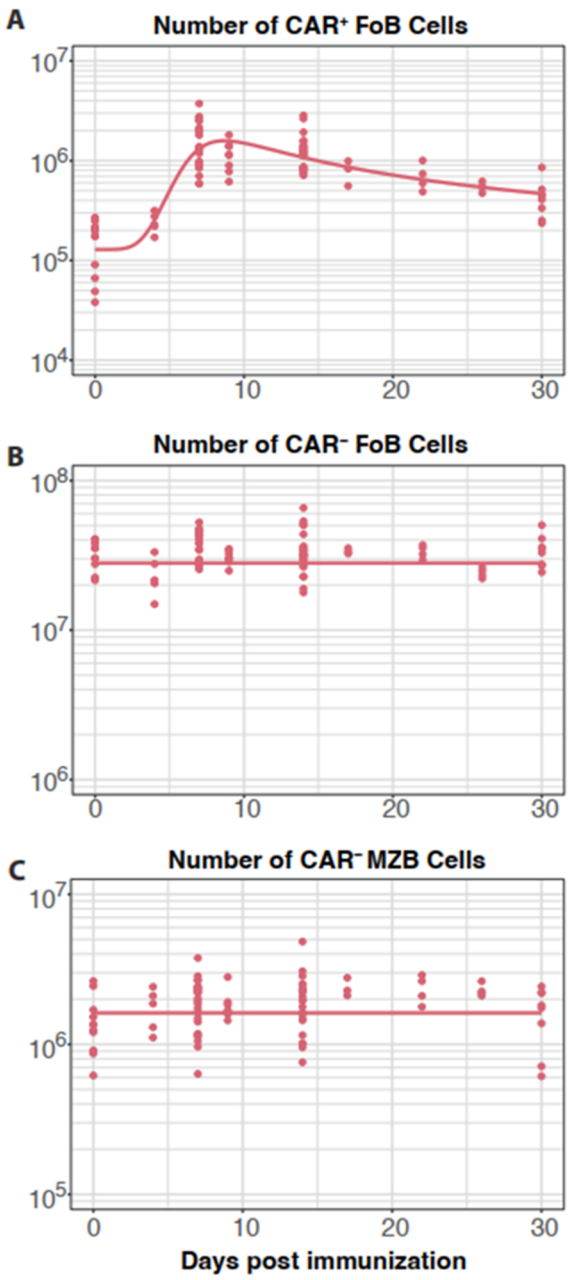

Fig. S8. Empirical descriptions of the dynamics of the numbers of FoB and MZB cells. We show here curves for CAR-expressing FoB cells, as well as CAR$^-$ FoB and CAR$^-$ MZB cells using the functions (defined in Text S2), which were used as inputs in our ODE model systems. The y axis depicts the total cell numbers of the respective cell population.

Supplementary Tables

Table S1. List of antibodies used in this study.

	Antibody	Conjugate	Clone	Company	Dilution factor
FACS	CD1d	Alexa Fluor 647	1B1	BioLegend	1:200
	TACI	APC	8G10-3	eBioscience	1:100
	CD86	APC	/	BD Biosciences	1:100
	CAR	FITC	sc-56892	Santa Cruz	1:25
	hCD2	FITC	REA972	miltenyi	1:50
	hCD2	PeVio770	/	miltenyi	1:100
	hCD2	APC; PE	RPA-2.10	eBioscience	1:100; 1:100
	CXCR4 (CD184)	PE	2B11	eBioscience	1:400
	CD43	Biotin; BV421	S7	BD Biosciences	1:350; 1:200
	CD38	PeVio770	/	miltenyi	1:100
	Streptavidin (SA)	PerCP; APC		BD Biosciences	1:100; 1:400
	B220	PerCP; APC; FITC; PE	RA3-6B2	BD Biosciences	1:100; 1:250; 1:200; 1:350
	BP-1 (Ly-51)	PE	BP-1	BD Biosciences	1:50
	CD24	Biotin	M1/69	BD Biosciences	1:800
	CD21	BV421	7G6	BD Biosciences	1:200
	CD23	PE; Alexa Fluor 647; PeVio770	B3B4	BD Biosciences	1:200; 1:100; 1:200
	CD5	BV421	53-7.3	BD Biosciences	1:200
	IgM	APC	II/41	BD Biosciences	1:100
	IgM	BV421; PeVio770	R6-60.2	BD Biosciences	1:100; 1:300
	AA4.1	PE	AA4.1	eBioscience	1:200
	CD95	BV421	JO2	BD Biosciences	1:200
	CD138	BV421	281-2	BD Biosciences	1:200
	Blimp1	PE	sc47732 PE	Santa Cruz	1:50
	Bcl6	Alexa Fluor 647	K112-91	BD Biosciences	1:50
	Irf4	eFluor660; PE	3E4	eBioscience	1:100; 1:500
	CD19	PeVio770	REA749	miltenyi	1:200
	CD19	BV510	1D3	BD Biosciences	1:200

	Notch2	PE	HMN2-35	BioLegend	1:180
	IgD	APC	11-26c.2a	BD Biosciences	1:300
ELISpot	rat-anti-mouse IgM	Biotin	R6-60.2	BD Biosciences	1:500
	rat-anti-mouse IgG1	Biotin	A85-1	BD Biosciences	1:500
	rat-anti-mouse IgG3	Biotin	R40-82	BD Biosciences	1:500
	Avidin D	HRP		Vector	1:2000
ELISA	rat-anti-mouse IgM	HRP	YF97	Southern Biotech	1:5000
	rat-anti-mouse IgG1	Biotin	A85-1	BD Biosciences	1:500
	Avidin D	HRP		Vector	1:2000
Histology	Rat-anti-mouse-hCD2	Biotin	RPA-2.10	BD Biosciences	1:50
	Rabbit-anti-mouse Laminin		L9393	Sigma-Aldrich	1:100
	Streptavidin	Alkaline Phosphatase		Sigma-Aldrich	1:200
	anti-Rabbit IgG	Peroxidase		Sigma-Aldrich	1:200
	Rat-anti-mouse CD90.2 (Thy1.2)	Biotin	53-2.1	BD Biosciences	1:100
	Rat-anti-mouse B220	APC	RA3-6B2	BD Biosciences	1:500
	Rat-anti-mouse Irf4		3E4	eBioscience	1:100
	Goat-anti-rabbit IgG	Cyanine Cy3		Jackson ImmunoResearch	1:500
	Goat-anti-rat IgG	Alexa Fluor 488		Jackson ImmunoResearch	1:500
	Streptavidin	Alexa Fluor 594		Life Technologies	1:500
	Rat-anti-mouse GL-7	FITC	GL7	BD Biosciences	1:100
	Rat-anti-mouse GL7	Alexa Fluor 647	GL7	BioLegend	1:100
	Rat-anti-mouse CD19	APC	1D3	BD Biosciences	1:200
	Rat-anti-mouse MOMA1	Biotin	ab51814	abcam	1:100

Table S2. Comparison of models describing population dynamics of MZB and GCB cell populations upon TD immunization. Relative statistical support for each model/sub-model is indicated as % model weights (see Text S3 for details on model weights estimation). The best-fitting combination is highlighted in green.

	Model weights %		
Model/sub-model	Neutral	Time-dependent loss of GC B cells	Time-dependent recruitment of FO B cells into GC
Branched	0.0	0.0	85.0
Linear	3.0	0.0	9.5
Null	0.0	0.0	2.5

Supplementary Text

Text S1. Mathematical models of B cell dynamics during a TD immune response

To model the emergence of CAR^+ MZB and GCB cells post immunization in control/CAR (which are rated as WT controls) and N2KO//CAR mice, we developed an array of system of ordinary differential equations (ODEs) that explored diverse pathways of B cell differentiation and logistics of their maintenance post activation. We observe no significant differences in the counts of CAR^+ MZB and GCB cells up to day 4 post immunization and therefore anchor the initial condition in all our models i.e. $t_0 = 4$ days. The details of the individual pathways and mechanisms that we tested are explained below. Model schematics are described in Fig. S7 above.

Text S1.1. Mechanisms of maintenance of GCB cells

We assumed that all GCB cells are derived from activation of FoB cells. The dynamics of CAR up-regulation in FoB cells post antigenic activation are unknown. Therefore, we assumed that activated FoB cells can directly become CAR^+ GCB cells or they flow into the CAR^- GC compartment prior to acquiring CAR expression. The rate of transition of CAR^- GCB to CAR^+ GCB cells is considered as an unknown parameter 'μ' in all our models. We explored modeling possibilities in which either the influx of cells into the GC compartment or their loss from the GC pool are varying with time post immunization.

1. Neutral dynamics. This is simplest model of constant birth-loss. We assume that the *per capita* rate of influx of FoB cells into GC 'α_1' and the net loss rate 'δ' of GCB cells remain constant with time. In our models, 'δ' is the balance between production of new GCB cells by cell division and their 'true loss' by death and differentiation.

2. Time-dependent loss of GCB cells. This model assumes that the net loss rate of GCB cells δ(t) varies with time post immunization. We explored a sigmoid form of δ(t), which allows for low loss rates early on during the growth phase of the GC reaction and relatively higher loss rate during the collapse phase.

$$\delta(t) = \frac{\delta}{1 + e^{-\nu\,(t-t0)^2}}. \tag{S1}$$

The influx of activated FoB cells into the GC compartment, 'α_1', is assumed to be constant in this model. Parameters ν and δ are unknowns in this model and are estimated from model fits, along with α_1.

3. Time-dependent recruitment of FoB cells into GC. In this model, we consider that the *per capita* rate of recruitment of FoB cells into the GC pool varies with time '$\alpha_1(t)$' and is defined as,

$$\alpha_1(t) = \frac{\alpha_1}{1 + e^{\nu\,(t-t0)^2}}. \tag{S2}$$

We allowed for high influx of FoB cells into the GC immediately post immunization, which then subsides over time. The net loss rate of GCB cells 'δ' is kept constant in this model is estimated doom the model fits along with ν and α_1.

<u>Text S1.2.</u> Loss of CAR$^+$ MZB cells

We assumed a constant *per capita* rate of net loss 'λ' for CAR$^+$ MZB cells. It has been shown that persistent Notch2 signaling is required for B cells to maintain their MZ status (Simonetti et al., JEM, 2013). Therefore, the net loss rate of MZB cells reflects the balance between their self-renewal (division) and their true loss via death, differentiation and deprivation of Notch2-dependent signals. In N2KO//CAR mice, activation of B cells leads to deletion of Notch2 and

thus increases the propensity of their loss by deprivation of Notch2-mediated signals. Therefore, we assume that the net loss rate of CAR^+ MZB cells in N2KO//CAR mice λ' to be higher than their net loss rate in control/CAR mice.

<u>Text S1.3.</u> Mechanisms of generation of MZB cells

We explored three different models – branched, linear and null – to explain the emergence CAR^+ MZB cells after TD-immunization.

1. Branched model: In this model, the antigen dependent activation of FoB cells induces a branch point in the B cell differentiation pathway, where some cells participate in GC reactions, while others acquire a MZB cell phenotype (Fig. S7A). Since the dynamics of CAR expression on FoB cells are unclear, we considered that activated FoB cells can differentiate into MZB cells before or after they express the CAR surface receptor. We assumed that activated FoB cells (irrespective of their CAR status) differentiate into CAR^+ MZB cells with a constant *per capita* rate 'α_2. The *per capita* rate of flow of cells from the CAR^- to the CAR^+ MZ compartment, 'α_3', was also assumed to remain constant. The total influx into MZB cells is then the sum of influx from FoB cells: α_2 times the pool size of the FoB compartment F(t) and the influx from CAR^- MZB cells: α_3 times the size of the CAR^- MZB compartment $M^-(t)$. The total size of the CAR-expressing FoB cell compartment varies with time post immunization. We independently modeled the pool sizes of CAR^+ FoB cells ($F^+(t)$) and CAR^- MZB cells ($M^-(t)$) (see Text S2 and Fig. S8) and used their empirical descriptions as inputs in our ODE systems. The size of the CAR^- FoB cell compartment (F^-) remains unchanged post immunization. We fixed the value of F^- to the mean of the spread in the numbers of CAR^- FoB cells across the whole experimental duration, which equals $e^{17.15}$.

In the branched model the dynamics for CAR^+ GCB (G^+) and CAR^- GCB (G^-) cells are identical between control/CAR and N2KO//CAR mice, but differ for CAR^+ MZB cells (M^+ and M^+_{N2}, respectively). The ODE system depicting the branched pathway is defined as,

$$\begin{aligned}
\dot{G^+} &= \alpha_1(t)\, F^+(t) + \mu\, G^- - \delta(t)\, G^+(t), \\
\dot{G^-} &= \alpha_1(t)\, F^- - \mu\, G^- - \delta(t)\, G^-(t), \\
\dot{M^+} &= \alpha_2\, (F^+(t) + F^-) + \alpha_3\, M^-(t) - \lambda\, M^+(t), \\
\dot{M^+_{\mathrm{N2}}} &= \alpha_3\, M^-(t) - \lambda'\, M^+_{\mathrm{N2}}(t).
\end{aligned} \tag{S3}$$

Total size of the GC pool (G(t)) is then derived by solving the ODE system and summing the time-courses of the sizes of $G^+(t)$ and $G^-(t)$ populations.

2. Linear model: This model follows a linear path in which activated FoB cells differentiate into GCB cells, which then subsequently give rise to CAR-expressing MZB cells. The schematic for the linear model is depicted in Fig. S7B. We assumed constant *per capita* rates of differentiation of GCB cells and CAR^- MZB cells into CAR-expressing MZB cells – 'α_2' and 'α_3' respectively. The ODE system of the linear pathway is given as,

$$\begin{aligned}
\dot{G^+} &= \alpha_1(t)\, F^+(t) + \mu\, G^- - \delta(t)\, G^+(t), \\
\dot{G^-} &= \alpha_1(t)\, F^- - \mu\, G^- - \delta(t)\, G^-(t), \\
\dot{M^+} &= \alpha_2\, G^+(t) + \alpha_3\, M^-(t) - \lambda\, M^+(t), \\
\dot{M^+_{\mathrm{N2}}} &= \alpha_3\, M^-(t) - \lambda'\, M^+_{\mathrm{N2}}(t).
\end{aligned} \tag{S4}$$

3. Null model: This model assumes that the CAR^+ fraction in MZB cells is purely derived from activation of pre-existing MZB cells and is maintained by activation induced continuous new deletion of the stop-cassette in CAR^- cells and by self-renewal of newly generated CAR^+ MZB cells (Fig. S7C). We defined that the *per capita* rate of daily new generation from the CAR^- to the CAR^+ MZB cell compartment as 'α_3'.

The ODE system of the null model is given as,

$$
\begin{aligned}
\dot{G^+} &= \alpha_1(t)\, F^+(t) + \mu\, G^- - \delta(t)\, G^+(t), \\
\dot{G^-} &= \alpha_1(t)\, F^- - \mu\, G^- - \delta(t)\, G^-(t), \\
\dot{M^+} &= \alpha_3\, M^-(t) - \lambda\, M^+(t), \qquad \text{here, } \alpha_2 = 0 \\
\dot{M^+_{\mathrm{N2}}} &= \alpha_3\, M^-(t) - \lambda'\, M^+_{\mathrm{N2}}(t).
\end{aligned}
\tag{S5}
$$

We highlighted the differences between the three ODE systems corresponding to each pathway that we tested in the blue text. The three sub models of GCB cell maintenance *viz.* neutral dynamics, time-dependent loss of GCB cells and time-dependent recruitment of FoB cells into GC, were tested within each ODE system.

<u>Text S2.</u> Defining phenomenological functions to capture the dynamics of precursor populations for the GC and CAR-expressing MZB cells

Dynamics of FoB cells: The total numbers of CAR-expressing FoB cells accumulate rapidly for up to a week after immunization and then decline gradually over time. We used the following empirical descriptor function to capture their dynamics using,

$$
F^+(t) = F_0^+ + (B_0\, t^n)\left(1 - \frac{t^q}{X^q + t^q}\right) \tag{S6}
$$

We estimated the parameters F_0^+, B_0, n, X, and q by fitting the equation to the log-transformed numbers of CAR-expressing FoB cells. The model fit is shown in Fig. S8A. The size of CAR$^-$ FoB cell pool remains constant for the whole duration of experimental period (Fig. S8B) and is given by the intercept = $e^{17.15}$.

Dynamics of CAR$^-$ MZB cells: The total numbers of CAR$^-$ MZB cells also remain unchanged and are given by the intercept = $e14$ (Fig. S8C). The total influx into the compartment is then given as product of *per capita* rate of influx and the instantaneous size of the precursor pool.

<u>Text S3.</u> Model ranking and selection criteria

We fitted each model (M_j) described in Text S1 simultaneously to the time-courses of cell counts of CAR^+ MZB cells, CAR^+ GCB cells and total B cells from control/CAR and N2KO//CAR mice. The model parameters (expressed as a vector θ) and the errors associated with the empirical measurements in each dataset (σ_i) are then estimated using the Bayesian statistical inference approach. We assumed that the residuals are normally distributed. The likelihood and the probability density for each dataset are then defined as,

$$\begin{aligned} y_i &\sim \text{Normal}(\mu_i, \sigma_i) && \text{[Likelihood]} \\ \mu_i &= M_j(\text{time}_i, \theta) && \text{[Model prediction]} \\ P(y_i|\theta) &= \frac{1}{2\pi\sigma^2}\exp\left(-\frac{(y_i-\mu_i)^2}{2\sigma^2}\right) && \text{[Probability density]} \end{aligned} \tag{S7}$$

We defined the 'prior' distributions of model parameters representing our assumptions regarding their values. The Bayesian procedure then updates the priors using the likelihood, to generate posterior distribution ($\hat{\theta}$) of model parameters conditional on the evidence from the data. The input for this procedure is the joint probability densities of three datasets.

$$P(\hat{\theta}|y_1, y_2, y_3) = \frac{P(y_1|\hat{\theta}) \cdot P(y_2|\hat{\theta}) \cdot P(y_3|\hat{\theta}) \cdot P(\theta)}{P(y_1) \cdot P(y_2) \cdot P(y_3)} \tag{S8}$$

Models are fitted using the no-U-turn-sampler (NUTS) sampler in the Stan programming language, where Parameters are sampled from the joint density P(θ) following Hamiltonian Monte Carlo algorithm (Stan Development Team, 2022). The descriptions of model systems, the prior distributions of parameters and the likelihood definitions are encoded in the Stan language and are available at the linked Github repository.

We compared the support for models using the leave-one-out (LOO) cross validation method, which estimates the expected log point-wise predictive density (elpd) for each model M_j – the measure of its out-of-sample prediction accuracy (Vehatari et al., Statistics and Computing 2016). We estimate the probability density of y_i given the model M_j fitted on the data with

observation i^{th} excluded → $P(y_i|y_{-i}, M_j)$. This leave-one-out process is repeated for all 'n' observations in the data. The elpd estimate and its standard error are then calculated as,

$$\widehat{\mathrm{elpd}_{\mathrm{loo}}^{j}} = \sum_{i=1}^{n} \mathrm{elpd}_{\mathrm{loo,\,i}}^{j} = \sum_{i=1}^{n} \log(P(y_i|y_{-i}, M_j),$$
$$\mathrm{se}(\widehat{\mathrm{elpd}_{\mathrm{loo}}^{k}}) = \sqrt{\sum_{i=1}^{n} \left(\mathrm{elpd}_{\mathrm{loo,\,i}}^{k} - \mathrm{elpd}_{\mathrm{loo}}^{k}/n\right)^2}. \tag{S9}$$

We used the *loo-2.0* package in the *Rstan* library to estimated elpd, which employs Pareto smoothed importance sampling (PSIS) (Vehatari et al., Statistics and Computing 2015) to approximate LOO cross validation. The estimates of elpd and its standard error were used to rank models using the Pseudo-Bayesian model averaging (BMA) method (Yao et al., 2018) implemented in the *loo-2.0* package. The model weight implies relative support for each model, analogous to the model weights calculated using Akaike's Information Criterion (AIC) (Akaike, 1978; Burnham, 2002; Wagenmakers and Farrell, 2004), and is given as

$$W_k = \frac{\exp\left(\widehat{\mathrm{elpd}_{\mathrm{loo}}^{k}} - \frac{1}{2}\mathrm{se}(\widehat{\mathrm{elpd}_{\mathrm{loo}}^{k}})\right)}{\sum_{k=1}^{K} \exp\left(\widehat{\mathrm{elpd}_{\mathrm{loo}}^{k}} - \frac{1}{2}\mathrm{se}(\widehat{\mathrm{elpd}_{\mathrm{loo}}^{k}})\right)}. \tag{S10}$$

As the models weight calculations are based on the elpd estimates from LOO cross-validation, it also denotes the confidence in model's ability to predict new data relative to all the other models considered in the analysis. Model weights for all the fitted models are shown in table S2 above.

Supplementary References

Besseyrias V, Fiorini E, Strobl LJ, Zimber-Strobl U, Dumortier A, Koch U, et al. Hierarchy of Notch-Delta interactions promoting T cell lineage commitment and maturation. J Exp Med. 2007;204(2):331-43.

Hampel F, Ehrenberg S, Hojer C, Draeseke A, Marschall-Schroter G, Kuhn R, et al. CD19-independent instruction of murine marginal zone B-cell development by constitutive Notch2 signaling. Blood. 2011;118(24):6321-31.

Casola S, Cattoretti G, Uyttersprot N, Koralov SB, Seagal J, Hao Z, et al. Tracking germinal center B cells expressing germ-line immunoglobulin gamma1 transcripts by conditional gene targeting. Proc Natl Acad Sci U S A. 2006;103(19):7396-401.

Heger K, Kober M, Riess D, Drees C, de Vries I, Bertossi A, et al. A novel Cre recombinase reporter mouse strain facilitates selective and efficient infection of primary immune cells with adenoviral vectors. Eur J Immunol. 2015;45(6):1614-20.

Simonetti G, Carette A, Silva K, Wang H, De Silva NS, Heise N, Siebel CW, Shlomchik MJ, Klein U. IRF4 controls the positioning of mature B cells in the lymphoid microenvironments by regulating NOTCH2 expression and activity. J Exp Med. 2013 Dec 16;210(13):2887-902. doi: 10.1084/jem.20131026.

Vehtari A, Gelman A, Gabry J. Practical Bayesian model evaluation using leave-one-out cross-validation and WAIC, Journal: Statistics and Computing, 2016 doi: 10.1007/s11222-016-9696-4

Vehtari A, Gelman A, Gabry J. Efficient implementation of leave-one-out cross-validation and WAIC for evaluating fitted Bayesian models, Journal: Statistics and Computing 2015 arXiv:1507.04544v1

Yao Y, Vehtari A, Simpson D, Gelman A. Using Stacking to Average Bayesian Predictive Distributions, Journal Bayesian Analysis 2018 https://doi.org/10.1214%2F17-ba1091

Hirotugu Akaike. On the Likelihood of a Time Series Model, Journal of the Royal Statistical Society 1978. Series D (The Statistician) Vol. 27, No. 3/4, https://doi.org/10.2307/2988185

Burnham KP, Anderson DR. , Model Selection and Multimodel Inference: A Practical Information-Theoretic Approach, 2002 Springer-Verlag, arXiv:1011.1669v3

Wagenmakers EJ, Farrell S. AIC model selection using Akaike weights, Psychon Bull Rev, 2004 DOI: 10.3758/bf03206482